Bi- and Multistatic Radar

Terje Johnsen and Karl Erik Olsen
Norwegian Defence Research Establishment (FFI)
P.O. Box 25
2027 Kjeller
NORWAY

Terje.Johnsen@ffi.no

ABSTRACT

Bi- and multistatic radar are expected to benefit from their separation of transmitter and receiver that denies receiver recognition by ARM, favours covered operation by their silent receivers, has higher detection possibilities of stealthy objects and is less vulnerable to jamming. The requirements of synchronisation in a separated transmitter-receiver system are discussed. The processing in bistatic radar must include the knowledge of geometry dependencies that exist for bistatic radar in range, Doppler and S/N ratio. Different track profiles relative to bistatic radar orientation and their range-Doppler relationships are presented together with examples from the processing in different types of bi- and multistatic radar. The extraction of target parameters, such as position, velocity and heading could require the combination of data as a function of time and/or contribution from several systems. A discussion of tracking in bi- and multistatic radar is included to the end that uses simulated input to estimate parameters with comparison of different methods of estimating measurement uncertainty and the use of bistatic or multistatic radar input data.

1.0   INTRODUCTION

Bistatic radar has been around since the early days of radar. Interest in bistatic radar in the post-war has been repeatedly reopened for periods of time [1]. New technological advances lead to new interest in looking at possible use of bistatic radar.

Before the invention of the duplexer, two antennas were necessary, one for transmission and one for receiving. The separation of the transmitter (Tx) and receiver (Rx) is the most obvious difference between monostatic and bistatic radars. Normally, a co-located Tx and Rx are not described as a bistatic system, even though they don't share a common antenna. As the separation becomes significant relative to the typical target range, effects that are typical to bistatic radar systems become relevant. These will be discussed in more details in the sections to follow.

The entities in bistatic radar, which is the Tx, Rx and target, could all in principle be located in either surface, air or space positions and they could be moving or fixed. This leads to a large matrix of possible combinations, which of not all are of practical use or will ever be studied. Within the scope of bistatic radar as defined in this paper, the source could be a radar transmitter of full control and well synchronized to the receiver, an uncontrolled radar source often named hitchhiking radar or a source not originally made for radar use such as various types of broadcast transmissions [2][3][4][14]. An illustration is shown in Figure 1 (a) to (c). The idea of using all available sources of transmission for target localisation is shown in a futuristic multiple source co-located receiver module in Figure 2.
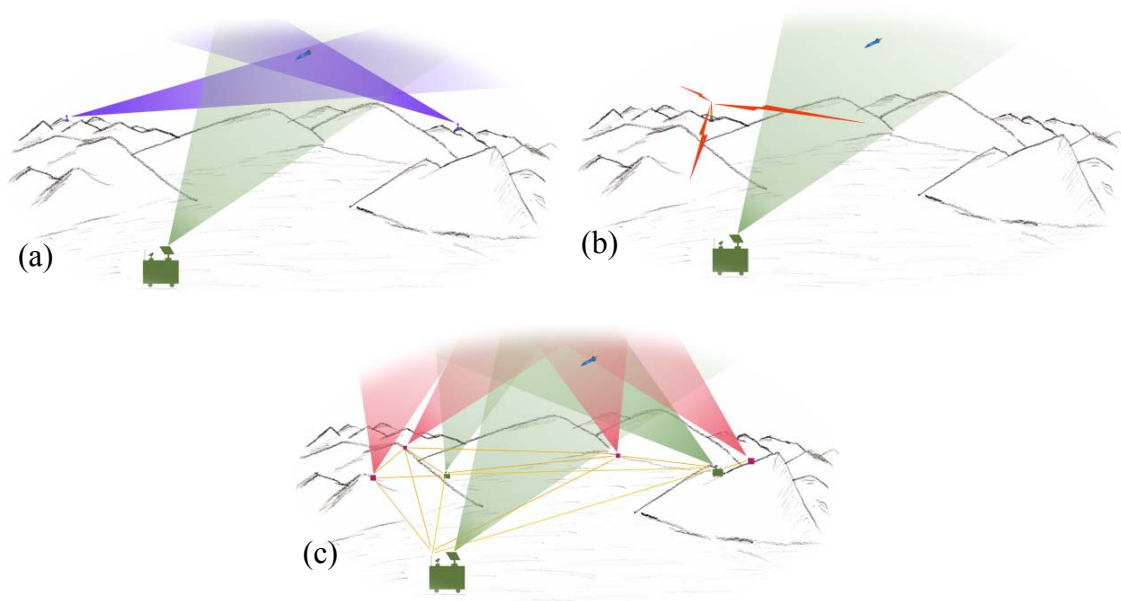
Figure 1: Bistatic radar based on different sources of illumination are shown in the plots (a), (b) and (c) for hitchhiking radar, broadcast transmitters and own well controlled radars, respectively.
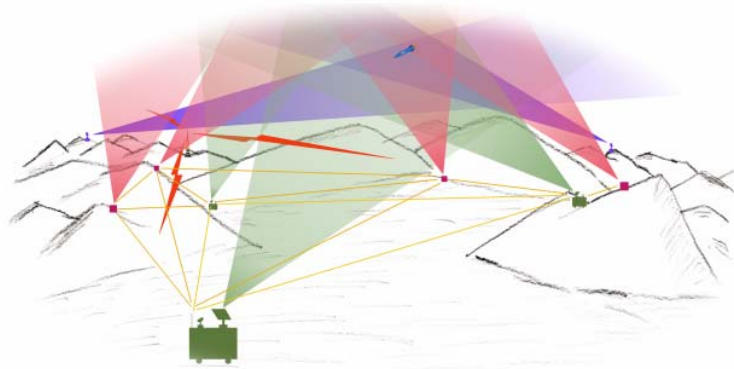

Figure 2: This plot illustrates the combined use of available sources in the process of producing the air picture.

Radars originally made for monostatic use could be added a bistatic mode by adding additional receivers spread out in the terrain as illustrated in Figure 3 or a set of netted radars could all operate in both mono and bistatic mode, adding increased complexity but also possibilities for better overall performance. A central issue in all use of bi- and multistatic radar is the topic of synchronization that will be discussed in section 3.0.

An obvious advantage of separating the receiver and the transmitter is that the receiver is passive and difficult to locate and which doesn't make it a target for e.g. Anti Radiation Missiles (ARM). Personnel are safe from ARM when located at the Rx. Separation also has effect on the effectiveness of Electronic Counter Measures (ECM) since the Tx and Rx are not co-located and therefore the Rx may be outside the main-lobe of the jammer or even outside Line Of Sight (LOS). Since the receiver is not readily discovered it is suitable for covert operations. Several receivers can operate without disclose of their positions with the transmitter stand off by a large distance. Relations of Signal to Noise ratio (S/N) will be discussed in 2.2 that explain the operation for this case.

Shaping of objects to reduce the backscattered energy towards the radar is believed to be less effective when bistatic radar is used. A higher on average bistatic Radar Cross Section (RCS) σ_b is expected for signal energy scattered in directions other than back to the transmitter location as in monostatic radar.
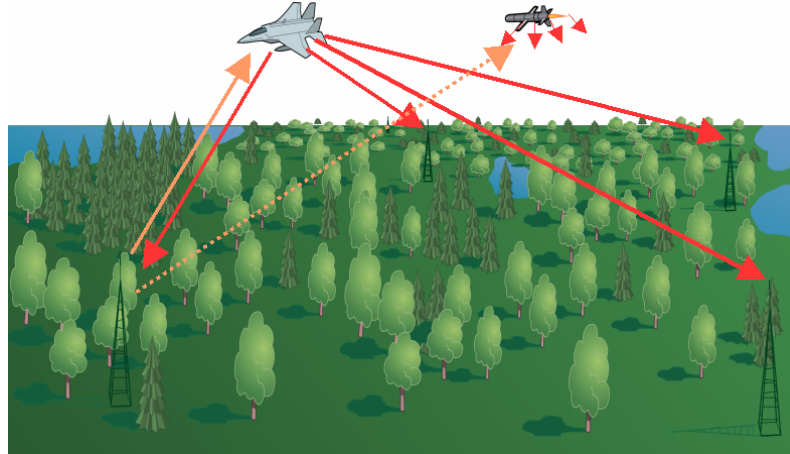

Figure 3: This figure shows a netted bi and monostatic radar system that collects the scattered energy towards a set of Rx units. Transmitter modes could also be co-located with receiver modes and in that sense operates both in monostatic and bistatic mode. (© FOI, Sweden)

2.0 BISTATIC GEOMETRY AND GEOMETRY DEPENDENT SIGNAL PROPERTIES

The separation of Tx and Rx introduces a range of modifications in a set of relationships normally viewed in monostatic radar. A set of central relations to bistatic radar processing will be discussed in the following sub-sections.

2.1 Bistatic Geometry and Isorange Contours

In bi- and multistatic radar, the transmitter (Tx) and receiver (Rx) pairs are generally separated a distance called the baseline of the system and denoted L as shown in Figure 4. A multistatic radar can be decomposed into a set of N bistatic Tx-Rx pairs. The position of Tx, Rx and target defines what is called the bistatic plane. So for each new target position a new bistatic plane is defined. In monostatic radar, the target range is found directly from measurements of the signal travelling time t from Tx to the target and back to the Rx. In bistatic radar the bistatic range or range sum

$$R = R_T + R_R \tag{1}$$

is found from t. R_T and R_R are now the distances from target to Tx and Rx, respectively. R_T is generally $\neq R_T$. To calculate R from t the Rx must know the exact transmission time t_0 that is it must be synchronized in time. To find all target positions that corresponds with this travelling time t, the position of Tx and Rx must be known.

A characteristic measure that describes the bistatic geometry is the bistatic angle β that is the angle between vectors from the target towards the Tx and Rx. The half of this angle is called the bistatic bisector labelled $\beta/2$ [1]. In calculations, the velocity component V of the target velocity V_{Tgt} in the bistatic plane is used. V has an angle δ towards the bistatic bisector as shown in Figure 4.
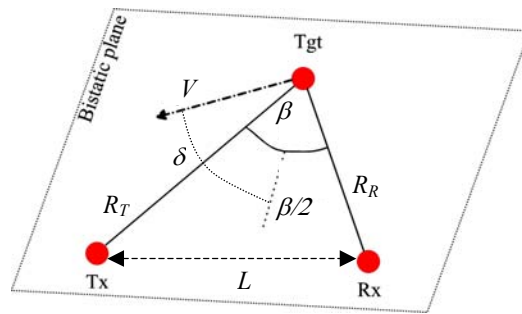
Figure 4: Bistatic geometry quantities in the bistatic plane defined by Tx, Rx and Tgt.

R could generally represent a target in any position on an ellipse in 2D or an ellipsoid in 3D as indicated by the coloured isorange ellipsoids in Figure 5 (a). Tx and Rx are in the focal points and the major axis is of size $a=R/2$. The blue ellipsoid barely pass the end of the Tx and Rx, which is due to a small excess distance travelled by the signal relative to the direct Tx-Rx transmission. For a given range resolution a closest range ellipsoid can be drawn, for which targets inside this bistatic range could not be separated in range from the direct signal. This region is sometimes called the blind zone or "evil eye". The green ellipsoid sections represent higher range sums well separated from the direct signal distance.
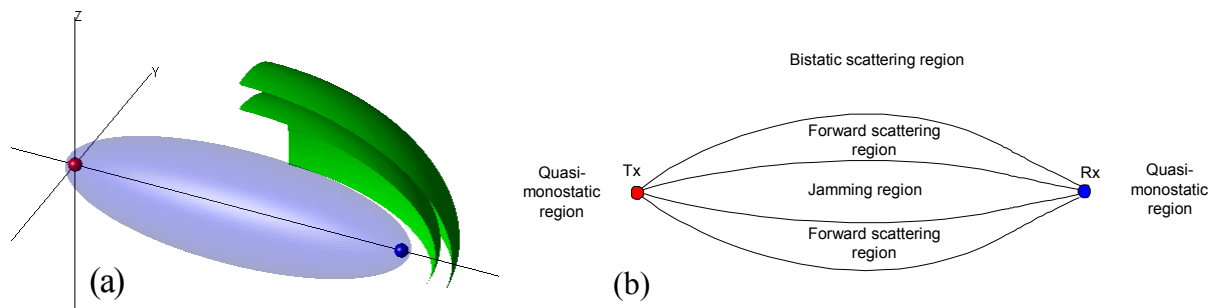

Figure 5: (a) Bistatic isorange ellipsoid in 3D shown in blue for a given range sum _R_. For other values of _R_ the ellipsoid size change as indicated in the green ellipsoid-sections for two larger ellipsoids. (b) Illustration of scattering regions in bistatic radar.

A sketch of the typical scattering regions is shown in Figure 5 (b). In the region between the Tx and Rx the transmitter is jamming the receiver. On the extended baseline outside Tx and Rx, the quasi-monostatic region is found where behaviour is monostatic except from the separation of Tx and Rx. The forward scattering region is found outside the jamming region and represent a region where enhanced RCS is expected. The remaining region is named the bistatic scattering region.

In Figure 6, a set of constant range sum ellipses with eccentricity defined as

$$e = \frac{L}{R_T + R_R} = \frac{L}{R} \tag{2}$$

is shown for $e=\{0.83,\ldots,0.33\}$. For $e=1$, the ellipse collapses into the baseline and in the other extreme when $e=0$, $R\gg L$ and it could be approximated by a circle as in the monostatic case.

In the same plot, a set of concentric hyperbolas is drawn that represent constant range difference contours of the difference $(R_T - R_R)$. Range difference measures from several radars (multistatic radar) or Time

Difference Of Arrival (TDOA) measurements e.g. in Electronic Support Measures (ESM) is the principle of operation in a multilateration system.
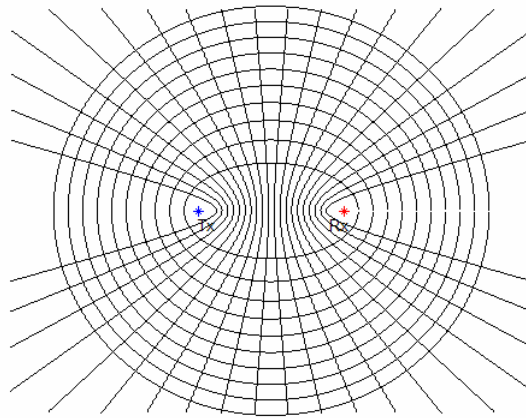

Figure 6: This plot shows a set of concentric isorange ellipse contours and a set of constant range difference in (R_T - R_R) hyperbola contours with Tx and Rx in the foci points.

A magnification of a section of Figure 6 is shown in Figure 7. It can be shown that all range difference hyperbolas are perpendicular to isorange ellipse contours crossing the hyperbola in all points. The tangent lines are drawn to indicate this. All hyperbola tangents coincide with a vector along the bistatic bisector $\beta/2$ for all positions. As seen in Figure 4, a target with a velocity vector in the direction of the hyperbola tangent will have δ=0 which will be shown in section 2.3 to correspond with the direction of maximum bistatic Doppler for that position. A target that moves along a hyperbola will have maximum Doppler for all positions along its track with respect to the bistatic radar. Since the isorange is perpendicular to the hyperbola, targets with velocity vector perpendicular to the hyperbola will result in zero Doppler.
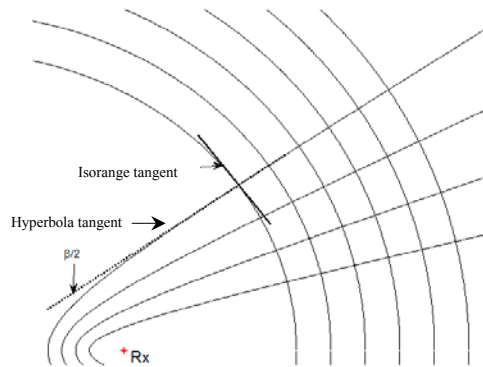

Figure 7: Magnification of a section from Figure 6, showing that isorange contours is perpendicular to hyperbola tangents for all hyperbola positions. The hyperbola tangent is also observed to collinear with the bistatic bisector $\beta/2$.

2.2   Bistatic Range Equation and Cassini Ovals

The bistatic range equation [1] is a modified version of the monostatic range equation given by

$$R_T R_R = \sqrt{\frac{P_T G_T G_R \lambda^2 \sigma_B F_T^2 F_R^2}{(4\pi)^3 k T_S B_n (S/N) L}} = \sqrt{K/(S/N)} \qquad (3)$$

where P_T is the transmitting power, G is the antenna gain, λ is the wavelength, F is the pattern propagation factor, σ_B is the bistatic RCS of the target, k is the Boltzman constant, T_S is the noise temperature, B_n is the noise bandwidth in the receiver, L is other losses and S/N is the signal to noise ratio. In the expression to the right in (3), K represents all parameters without S/N. If the S/N value is the minimum detection threshold value, the maximum range product of the system could be found. The subscript T and R refer to quantities related to the Tx or Tx to target path and Rx or Rx to target path, respectively.

It can be recognized that (3) is of the form of Cassini ovals [5] defined by

$$r_1 r_2 = b^2 \tag{4}$$

which defines a contour that has a constant range product from two points that are located a distance L apart. In bistatic radar these points are centred on Tx and Rx. For a given S/N ratio, a constant range product contour can be drawn as shown in a 2D cut in Figure 8. K in (3) has been set to a constant value for the calculations of the Cassini ovals. These curves are typically not cocentric with the isorange contours leading to a variation in S/N ratio along a constant range sum R contour. We also observe that the ovals collapse into two parts as the ratio is increased. This occurs when the contour passes the midpoint between Tx and Rx, that is when $r_1=r_2=L/2$. From equation (4) we then see that $b=L/2$. The Cassini ovals breaks into two similar separate ovals located around Tx and Rx when $b<L/2$ and forms one connected oval contour for $b>L/2$. Summarized it can be written as:
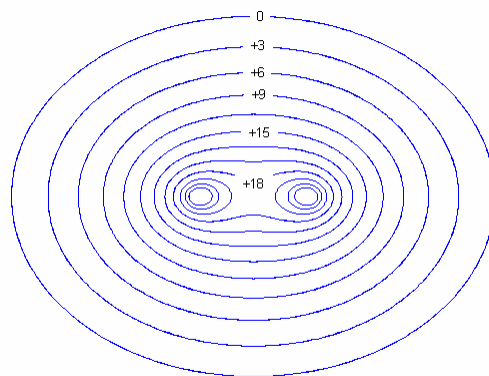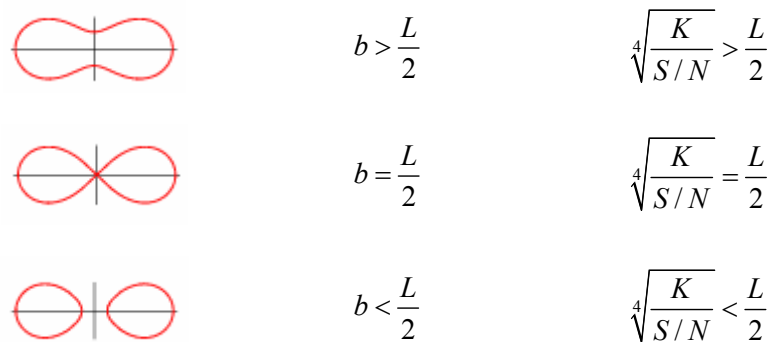
$$b > \frac{L}{2} \qquad \sqrt[4]{\frac{K}{S/N}} > \frac{L}{2}$$

$$b = \frac{L}{2} \qquad \sqrt[4]{\frac{K}{S/N}} = \frac{L}{2}$$

$$b < \frac{L}{2} \qquad \sqrt[4]{\frac{K}{S/N}} < \frac{L}{2}$$

Figure 8: This plot shows Cassini-ovals for a set of S/N ratios with relative intervals of 3dB.

A 3D plot of the continuous change in S/N ratio for targets in the plane of the Tx and Rx is plotted in Figure 9. The spatial variation in S/N is obtained by rotating the ovals in Figure 8.
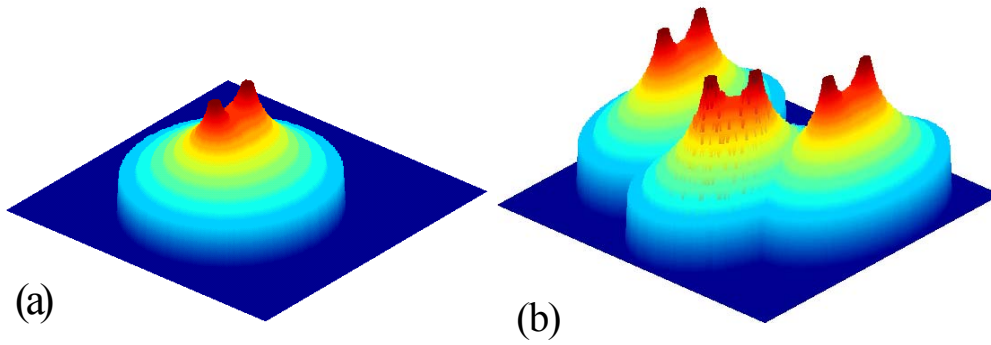
Figure 9: (a) This 3D plot is a mapping of the S/N ratio in bistatic radar for various target locations. A limitation on the calculation area has been used as observed by the end of the light blue colour. (b) This plot shows the combined S/N ratio map for a target in the area as observed by three bistatic radars. Maximum S/N ratio for all radar sets has been used at all target positions.

Depending on the system in mind, the operation region could be restricted to two isolated oval regions, which is the case with a powerful standoff Tx, or be restricted to a connected region limited by a lower *S/N*. The combination of several systems results in a combined region that is dependent on geometry as indicated in Figure 9 (b). In the arguments above, a constant value of the parameters represented by *K* has been assumed. If for instance the target RCS is reduced, *K* decreases and the oval of constant *S/N* ratio would shrink.

2.3   Bistatic Doppler

The frequency shift resulting from motion of either target or one of the transmitter or receiver is different from what is observed in monostatic radar. In monostatic radar, the Doppler shift $f_{d,m}$ is found from the velocity component v_M of the target towards the single co-located Tx and Rx. The bistatic Doppler shift $f_{d,b}$ are generally described by contribution of range rates in both R_T and R_R as

$$f_{d,b} = \frac{1}{\lambda}\left(\frac{dR_T}{dt} + \frac{dR_R}{dt}\right)$$
(5)

The range rates can be expressed by the target velocity V in the bistatic plane, bistatic bisector $\beta/2$ and the angle δ [1], resulting in the expression

$$f_{d,b} = 2\frac{V}{\lambda}\cos(\delta)\cos(\beta/2)$$
(6)

In the special case $R_M = R_T = R_R$, the well-known monostatic Doppler shift results:

$$f_{d,m} = 2\frac{v_M}{\lambda} = 2\frac{dR_M/dt}{\lambda},$$
(7)

When the velocity vector of the target or the component V in the bistatic plane is along the bistatic bisector, $\delta=0$. From (6) we then observe that the bistatic Doppler shift has its maximum when $\beta=0$, that is when the target is on the extension of the baseline. This target direction is named the quasi-monostatic region as shown in Figure 5 (b). For all other values of β, the shift in frequency is reduced with reference to monostatic radar. Figure 10 (a) shows the distribution of the bistatic angle β for all target positions in
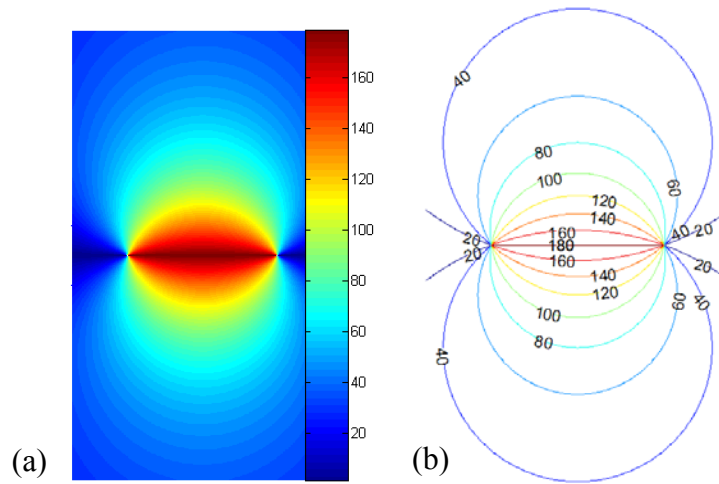
(a)   (b)

Figure 10: (a) This plot shows a two-dimensional view of the distribution of the bistatic angle β in the bistatic plane. The transmitter and receiver are located in the focal points of the image. (b) Constant β contours in bistatic geometry plotted with contour lines at an interval of $\Delta\beta$=20 degrees.

A constant bistatic angle contour results in circle sections that terminate in the Tx and Rx positions as shown in Figure 10 (b) for a series of β values.

From equation (6) we observe that the velocity component that determines the Doppler shift is the projected velocity component of the target along the bistatic bisector, $V\cos(\delta)$, onto either the R_R or R_T. The factor $\cos(\delta)\cos(\beta/2)$ in (6) can be viewed as a bistatic Doppler reduction factor with reference to a maximum value found for $f_{d,b}(\beta=0,\delta=0)$. In Figure 11, $\cos(\delta=0)\cos(\beta/2)$ is plotted as a function of target position in the bistatic plane when we assume that δ=0 for all values of β, which is equivalent to the velocity vector component in the bistatic plane being parallel to $\beta/2$. From the computation we observe that along the extension of the baseline, outside Tx and Rx, we get as expected a reduction factor of 1. This represents an unchanged Doppler in this quasi monostatic direction. At the baseline $\beta/2=90$, and a factor of zero is found. The Doppler shift is therefore zero for all velocities and target positions on the baseline. This is a general result for all values of δ.
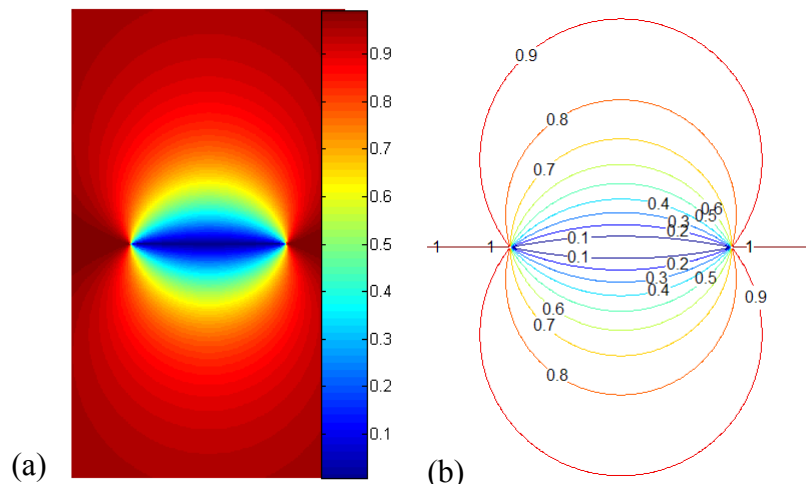
(a)

(b)

Figure 11: (a) Continuous mapping of reduction factor as a function of target position. (b) Doppler reduction factor cos(β/2)cos(δ=0) contour curves as a function of position in the bistatic plane.

The magnitude of the recorded Doppler shift is also modulated by the $\cos(\delta)$ factor with a positive shift for $\delta = [-90,\ldots,90]$ and negative Doppler for $\delta \neq [-90,\ldots,90]$. Zero Doppler is found when $|\delta| = 90$. This is equivalent to a velocity vector that is normal to the bistatic bisector, which as mentioned before is the case for a target that moves tangential to a bistatic isorange contour.

2.4   Doppler and Velocity for Flight Profiles

To understand how typical flight profiles will affect the recorded bistatic Doppler and velocity estimate, a series of flight profiles have been simulated. To ease the understanding, simulations have been executed with tracks manoeuvring in a 2D North-East coordinate system. The profiles labelled P1, P2, P3 and P4 are shown in Figure 12. In P1, the targets have a linear flight profile parallel to the baseline of length L. The Tx and Rx are located on the East-axis and the target profiles are simulated for four different distances from the baseline in the North direction of magnitude L/2, L, 3L/2 and 2L. The second set P2, has flight profiles perpendicular to L but outside the baseline, as shown with red dotted lines in Figure 12. The set consists of four linear tracks with an East coordinate of L, 2L/3, 2L and 5L/2. The third track set, P3, is parallel to P2 but these cross the baseline. The last flight profiles P4 are circular tracks centred on the middle of the baseline with circle radius of L, 2L and 3L.
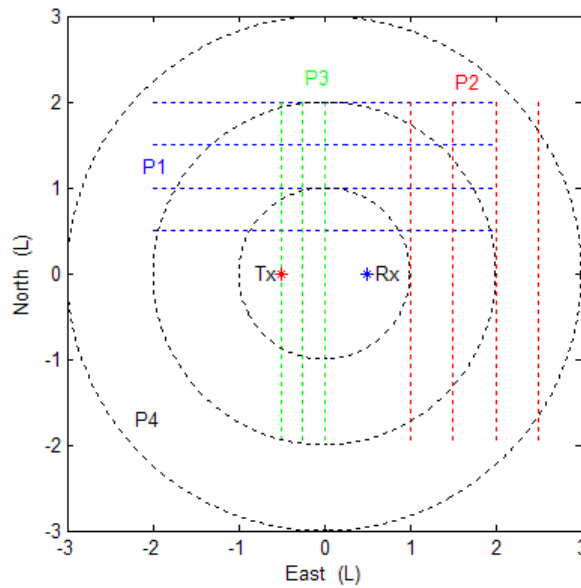
Figure 12: Flight track sets P1, P2, P3 and P4 in a bistatic geometry.

With the four sets of flight profiles described above, different measures will be presented that captures essential geometry dependent properties. In calculations of the Doppler shifts and estimation of a velocity a target velocity of 100 m/s and a carrier frequency f_{Tx} = 10 GHz were used for all track profiles.

2.4.1   Track Profile P1 Analysis

These track profiles generally don't follow bistatic isorange contours or constant S/N ratio contours (Cassini Ovals). In Figure 13 (left), the variation of β is shown as a function of East coordinate given in baseline units L for each of the four tracks. β is symmetric about the centre of the baseline and has a maximum value for *East = 0*. Both β and δ are non-linear functions of East coordinate and the resulting Doppler reduction factor plotted to the right in Figure 13 shows clearly a nontrivial function with three points of inflection that become more observable at closer ranges.

The bistatic Doppler is calculated from (6) for each position along the tracks. In the receiver, the range sum R is found from knowledge of transmission times. When the bistatic radar don't have restricted lobe widths or detailed information of their pointing direction, half the range sum *(R/2),* are used as the range in a Range-Doppler plot. In Figure 14 (left), an estimate of the target velocity component in the bistatic plane along the bistatic bisector given by

$$v_{M\_\beta/2} = \frac{cf_{d,b}}{2f_{Tx}}$$

(8)

is plotted as a function of half the range sum normalized by the baseline, *(R/2)/L*. From (6) we see that this is equivalent to β=0, which is the monostatic case and the reason for the subscript M in the velocity name. The reference point is now located in the middle of the baseline.

Alternatively, if the bistatic radar has knowledge of its beam directions and an assumption is made that the target is located at the bore sight of the beam, β could be calculated along with a value for the receiver to target range R_R. With this information the, $V\cos(\delta)$ term named $v_{\beta/2}$ can be calculated as

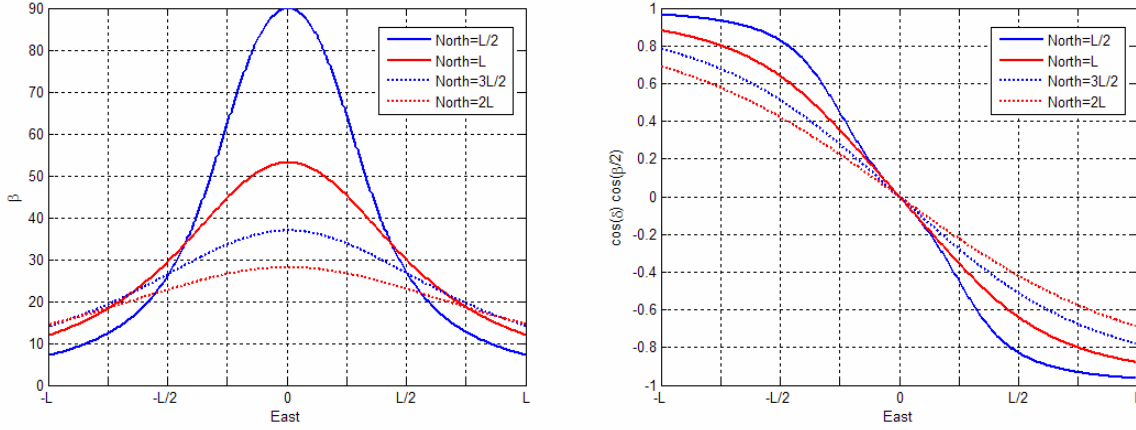$$v_{\beta/2} = \frac{cf_{d,b}}{2f_{Tx}}\cos(\beta/2) \tag{9}$$

Figure 13: Left: This plot shows the bistatic angle β as a function of distance in East direction for the four tracks with North coordinates $L/2$, L, $3L/2$ and $2L$. Right: Doppler reduction factor $\cos(\delta)\cos(\beta/2)$ as a function of East coordinate along tracks.
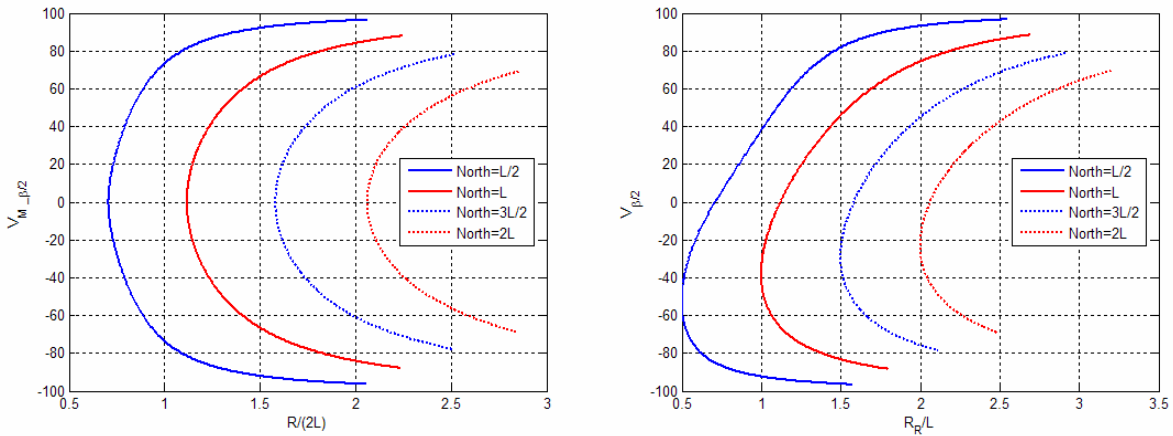

Figure 14: Left plot shows the velocity estimate $v_{M\_\beta/2}$ of the target as a function the normalized half range sum. Right plot shows the velocity component $v_{\beta/2}$ of the target along $\beta/2$ as a function of normalized receiver to target range.

To the right in Figure 14, $v_{\beta/2}$ is plotted as a function of the R_R normalized by the baseline L. Since the range reference point now is the receiver, we observe correctly that the position of zero Doppler don't coincide with the minimum range. The minimum range is found when the Doppler is negative since $\delta > 90$. For both plots in Figure 14 it's observed that the range-Doppler behaviour becomes closer to single curvature curves when the distance to the baseline increases. When $L<<R$ or R_R we approach the monostatic case.

2.4.2   Track Profile P2 Analysis

These tracks are perpendicular to the tracks in P1 and to the baseline. They belong to a class of tracks that don't cross the baseline. It consists of four tracks with East coordinate L, $2L/3$, $2L$ and $5L/2$. Symmetry is

expected around crossing of an extended baseline as seen in Figure 15. To the left, β is shown as a function of North coordinate which has a maximum for

$$North = \pm\sqrt{East + East^2} \tag{10}$$

This maximum can be understood from Figure 10 (b). The Doppler reduction factor shown to the right in Figure 15 shows symmetry about *North=0* with a sign shift from positive to negative Doppler.
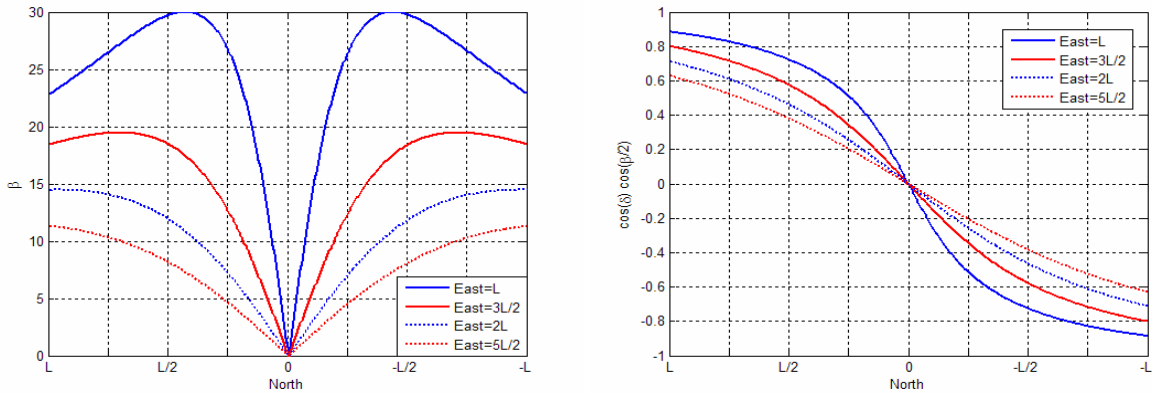

Figure 15: Left: This plot shows the bistatic angle β as a function of distance in East direction for the four tracks with East coordinates *L*/2, 3*L*/2, 2*L* and 5*L*/2. Right: Doppler reduction factor cos(δ)cos(β/2) as a function of East coordinate along tracks.

In Figure 16, the two different Range-Doppler plots are shown. The bistatic angle is quite small along these tracks as observed to the left in Figure 15, and therefore a less pronounced difference in velocity is observed. The two plots have curves of similar character.
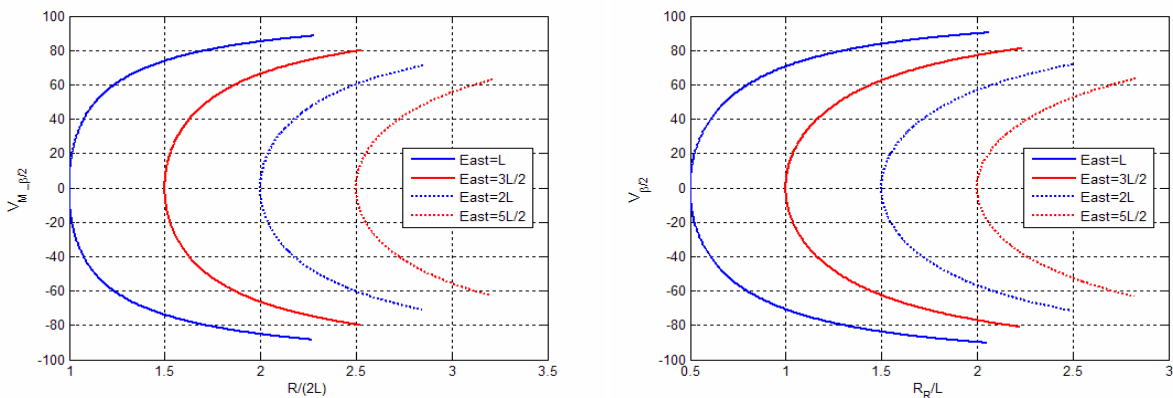

Figure 16: Left: Velocity estimate $v_{M\_\beta/2}$ of the target as a function the normalized half range sum. Right: Velocity component $v_{\beta/2}$ of the target along β/2 as a function of normalized receiver to target range.

2.4.3   Track Profile P3 Analysis

The P3 tracks have the same direction as the P2 tracks, but they cross the baseline between Tx and Rx. There are three tracks in this set, one is crossing the middle of the baseline (*East=0*), one is crossing directly through Tx (*East=-L/2*) and the last has an *East* coordinate between these two.

To the left in Figure 17, we observe that the maximum β is found at the crossing of the baseline. The $\cos(\delta)\cos(\beta/2)$ factor to the right has the same curvature as P2 but with a steeper slope close to origin and a discontinuity when it directly crosses the Tx position.
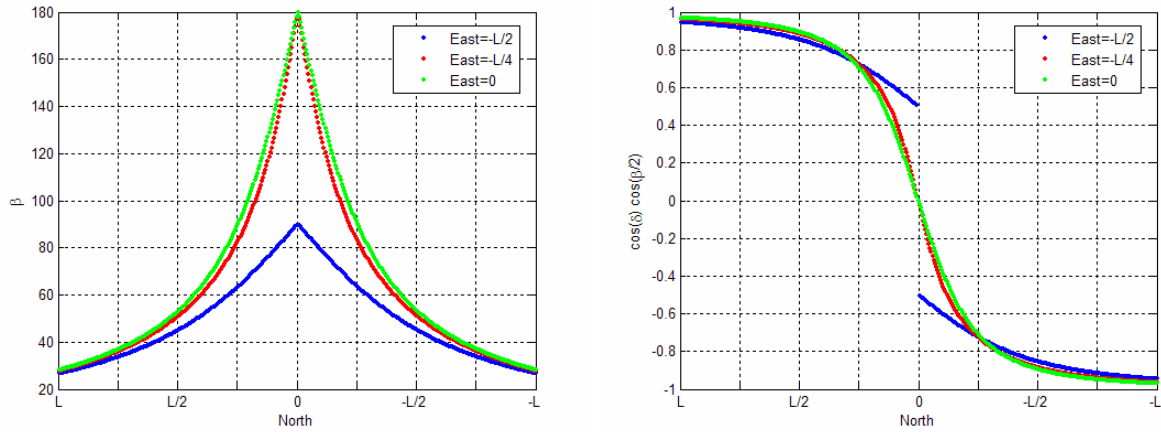
Figure 17: Left: This plot shows the bistatic angle β as a function of distance in East direction for the four tracks with East coordinates -L/2, -L/4, and 0. Right: Doppler reduction factor cos(δ)cos(β/2) as a function of East coordinate along tracks.

For the track with *East=0* the velocity is perfectly aligned with the bistatic half angle. This leads to an exact velocity value when incorporating knowledge of $\beta/2$ as seen to the right in Figure 18 (green line). For the quasi-monostatic velocity estimate shown to the left, an offset from the correct value is found.
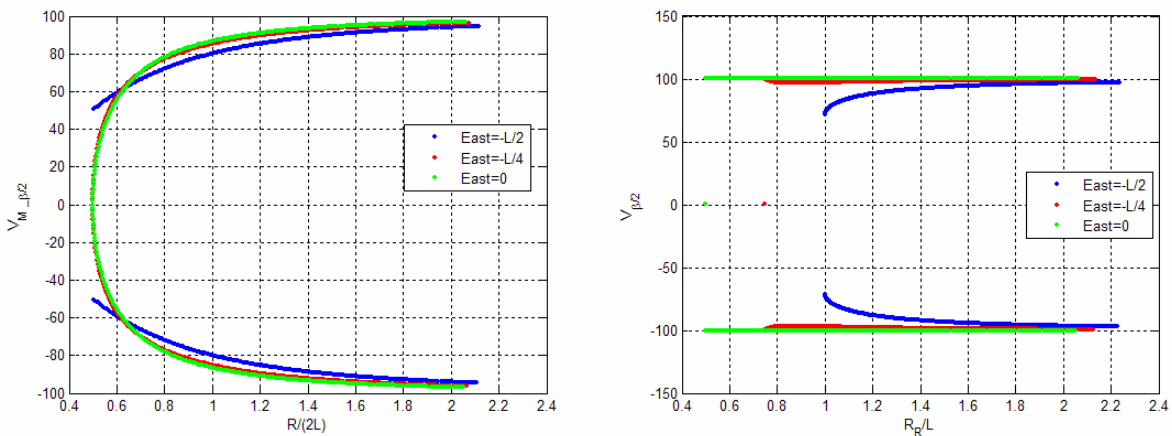
Figure 18: Left plot shows the velocity estimate $v_{M\_\beta/2}$ of the target as a function the normalized half range sum. Right plot shows the velocity component $v_{\beta/2}$ of the target along $\beta/2$ as a function of normalized receiver to target range.

2.4.4   Track Profile P4 Analysis

The last track profiles are a set of three concentric circles centred in the origin. Their radiuses are set to L, $2L$ and $3L$. To the left in Figure 19, β is plotted as a function of rotation angle θ_R. We observe that max($\beta/2$) is found for θ_R =90 and θ_R =270 and it decreases as a function of increasing radius. For large

ranges the isorange ellipses approaches a circle, and since a velocity component in the bistatic plane that is parallel to these isorange ellipses result in zero Doppler, a reduced Doppler factor is found for an increasing radius as observed to the right in Figure 19.
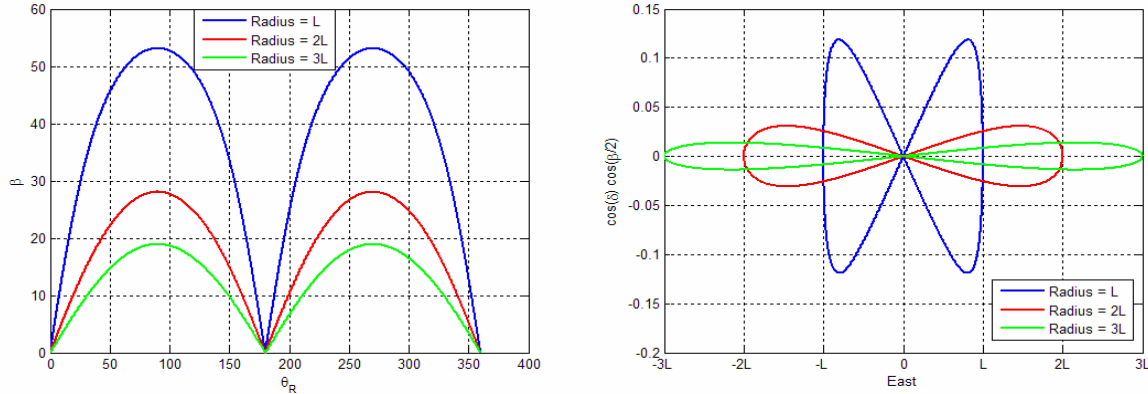

Figure 19: Left: This plot shows the bistatic angle β as a function of rotation angle θ_R. for the three tracks with radius L, $2L$ and $3L$. Right: Doppler reduction factor $\cos(\delta)\cos(\beta/2)$ as a function of East coordinate along tracks.

For all circles of all ranges there will be exactly four angles θ_R=0, 90, 180 and 270, where this circle is tangential to an isorange ellipse and consequently resulting in zero Doppler. In Figure 20, the velocity is estimated and these four zero bistatic velocities could be found. For the left plot the Range-Doppler relationships result in two ellipses collapsing on top of each other due to range symmetry around origin, while the right plot spreads this relationship out in a "butterfly-pattern". In this plot the range R_R relates to the receiver and therefore the two turns don't fall on top of each other.
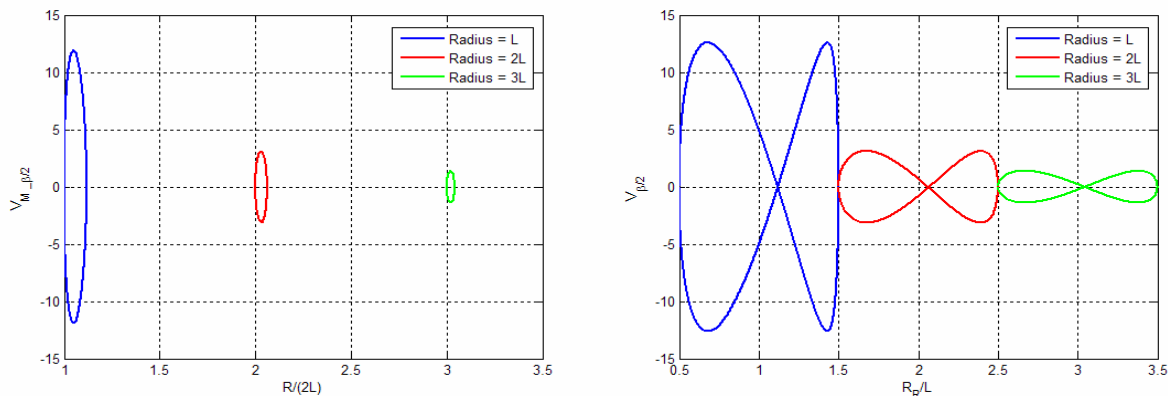

Figure 20: Left plot shows the velocity estimate $v_{M\_\beta/2}$ of the target as a function the normalized half range sum. Right plot shows the velocity component $v_{\beta/2}$ of the target along $\beta/2$ as a function of normalized receiver to target range.

In these analyses the transmitter and receiver both had fixed positions. If Tx, Rx or both have a velocity, these have to be encountered for in the range rates of equation (5). The maps of iso-Doppler contours depend on the velocity vectors and will take on specific patterns depending on the very details in each case [1].

3.0 SYNCHRONIZATION

In bi- or multistatic radar the distance between transmitter and receiver units can be extensive and establishing a common time and frequency reference by means of cable or fiber could be difficult. Alternatively, a communication link could be used with line of sight coverage towards all units as a kind of direct synchronization.

The frequency device that provides the precise time and frequency is usually a local reference oscillator of some sort in both bi- and monostatic radar. To maintain time and frequency synchronization in a separated Tx and Rx configuration where no direct synchronization is practical, stable local oscillators are often used. Due to aging, temperature variations and other environmental influence, the frequency will not be constant over time. A range of various qualities can be purchased ranging from quartz oscillators, temperature controlled quarts with single or double ovens for stable operating temperature, to more expensive atomic clocks such as Rubidium or Cesium oscillators.

Due to the inherent instability, re-synchronization must be carried out on a time interval depending on specified stability and synchronization requirements. The stability directly influences the coherent integration time in a system. Another important aspect of reference oscillators is their noise characteristics. Phase noise is specified in frequency domain for given offsets in frequency from the carrier e.g. –110 dBc at 10Hz and/or in time domain by the two-point variance (Allan variance) for a set of time intervals. Low phase noise close to the carrier is important in Doppler processing in order to detect slow-moving targets with small Doppler shifts. Additional noise degradation is a problem if mounted on a vibrating platform, such as an airplane, and attention must be paid on the degraded phase noise spectrum.

Indirect synchronization of local references has for instance been used in our experimental multistatic radar by use of local oscillators disciplined by GPS. The GPS also provides a high quality time tick, the 1 Pulse Per Second (1PPS) signal that is used for timing pulse transmission and range estimation. In GPS receivers the uncertainty in time is in the order of 100ns or less. The local oscillator determines the short time stability, while the long time stability is disciplined to the stability of the GPS satellites atomic clocks. As long as the receiver is locked to the GPS, the long time stability is ensured. In the case of GPS-jamming or receiver unlock, the stability of the local oscillator unit will determine the drift due to aging and temperature changes etc.

4.0 EXAMPLES OF PROCESSING IN BI- AND MULTISTATIC RADAR

A wide range of bi- and multistatic radar systems has been reported. These range from conventional radar systems with well controlled Tx and Rx units to hitchhiking radars and use of non-radar source signals in so called Passive Coherent Location (PCL) systems. At FFI two experimental ground-based bi- and multistatic radar systems have been used recently for experimental purposes. One of the systems uses a non-cooperative rotating 2D radar as source and a receiver equipped with an omnidirectional antenna, discussed in 4.1. All details of transmission are not known, such as rotation times, PRFs etc. and estimation of these parameters are part of the processing. The second multistatic radar uses synchronized Tx and Rx units with restricted antenna lobe widths, see section 4.2.

4.1 Bistatic Radar with Non-Cooperative Tx

The use of a non-cooperative Tx requires the estimation of the lobe direction as a function of time, $\varphi(t)$. With an omnidirectional Rx antenna that gives no angle information on the detections, direction estimates of detections are given relative to Tx. For detection at a bistatic range R, target positioning is determined by the Tx angle of transmission $\varphi(t)$, the Tx antenna beam-width and the bistatic isorange contour of range R. In Figure 21, an illustration of the intersection of the Tx beam and the isorange contour is shown for a
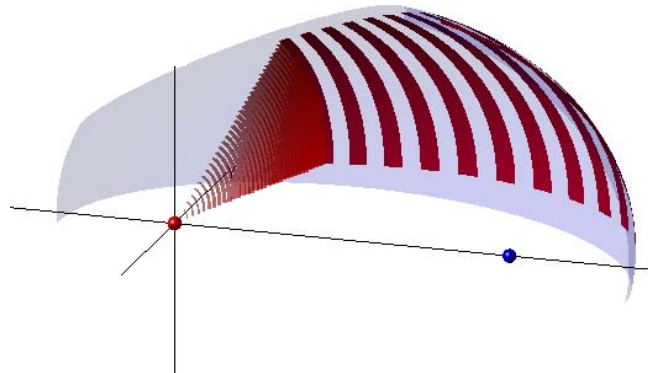
**Figure 21: Illustration of bistatic radar system-I with known transmit angle
and small azimuth angle beam width and about 30 degrees elevation
beam width. A part of an isorange ellipsoid is drawn in light blue.**

Depending on $\Delta\theta_{el}$ and the ratio R/L, the R_T range uncertainty $\Delta R_T(\varphi)$ change is a function of direction angle φ, as shown in Figure 22. No analytical expression is given for $\Delta R_T(\varphi)$, but from Figure 21 it is observed that the red band is a part of an ellipse when $\varphi=0$ and 180 and part of a circle when $\varphi=\pm90$.

To analyse $\Delta R_T(\varphi)$, ten flight paths were analysed in the Tx-Rx plane at distances from the baseline of

$$y/L = \{0.1, 0.2, \ldots, 1\} \tag{11}$$

as shown in Figure 22. The transmitter and receiver sites are shown with red and blue circles, respectively. For each distance, $\Delta R_T(\varphi)$ is plotted for each position along the flight track. At each (x,y) position, $\Delta R_T(\varphi)$ is found from the cross-section of the isorange ellipsoid in (x,y) and the plane defined by the Tx beam, assuming $\Delta\theta_{az}=0$ and limited by $\Delta\theta_{el}$. The colour bar represents the magnitude of the relative change in $\Delta R_T(\varphi)$ with colours spanning from blue (small) to red (large) for each track separately. We observe that the largest uncertainty is found when $y/L=0.1$. This is understandable as the minor axis b of the ellipsoid becomes small relative to L. With a constant $\Delta\theta_{el}$, the range uncertainty becomes L when $y=0$ for a target on the baseline, which corresponds to a collapsed ellipsoid with $b=0$.

A plane with a normal vector parallel to the baseline will have a circular cross-section with the isorange ellipsoid for all x positions. This explains why there is a range uncertainty of zero when the targets pass $x=0$. For all other x positions the cross-section forms a curve that is neither part of a circle nor an ellipse except for target positions along the extended baseline. On the interval $x/L=<-0.5,\ 0>$, the range increase when $\theta_{el}>0$ relative to the range value of $\theta_{el}=0$. This is due to the curvature of the circle with Tx in origin (zero range uncertainty) being larger than the curvature of the ellipse section for that direction and elevation. If these detections should be fed to a tracking filter, an expression that describes the extension of the uncertainty volumes should be used in the filtering process.
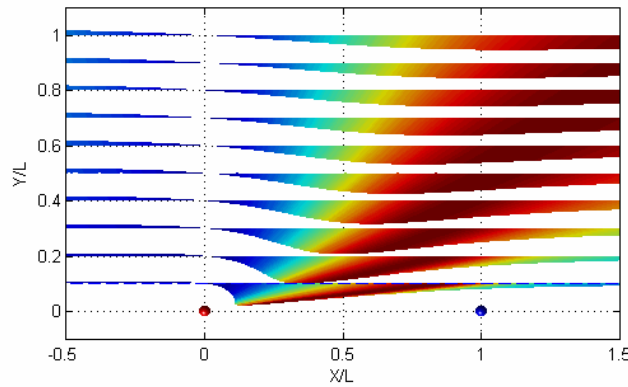
Figure 22: Range uncertainty as a function of distance from baseline and transmitter-target angle. The colours for the range span found for different target positions are used to ease the view of the changing range uncertainty (blue is small and red is large).

To position detections, an estimate of $\varphi(t)$ must be found and the position of Tx and Rx must be known. If there is LOS between Tx and Rx, we assume that the direct pulse at $\varphi=\varphi_0$ has the highest intensity when the antenna in Tx points towards Rx. From data recorded for a whole scan period of the Tx antenna t_{scan}, an estimate of the angle φ_0 can be found. For a high power radar or short baseline radar, direct pulses and scattered energy from objects at other ranges can be detected for all pointing directions as shown in Figure 23. Here, the signal is plotted as a function of time and excess range relative to the time of the incoming direct pulse that always has travelled a distance L. As a function of time, peaks are observed that we assume correspond with $\varphi=\varphi_0$.
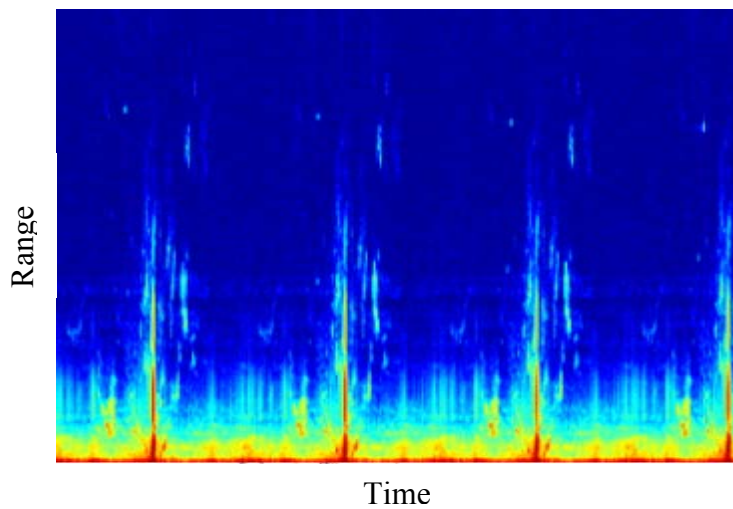

Figure 23: Signal strength of sampled signal for an excess range calculated relative to the incoming direct pulse as a function of time for more than four scans of the Tx beam.

From observations of several scans, $\varphi(t)$ could be estimated by

$$\varphi(t) = \varphi_0(t_0) + \left(\widetilde{\frac{d\varphi}{dt}} \right)(t - t_0) \qquad (12)$$

where φ_0 is the angle when Tx points along the baseline towards Rx, t_0 is the time corresponding to φ_0 and $\dfrac{\widetilde{d\varphi}}{dt}$ is an estimate of the current angle rate of the Tx antenna.

Before the sampled signal $S(t_i)$ could be further processed, the arrival time $t_{p,j}$ of direct pulse j must be estimated. When all direct pulses P_j are analysed, changes in PRF could be found as shown for a section of a recorded data set in Figure 24. The number of pulses j changes from scan to scan according to the detailed PRF staggering scheme.
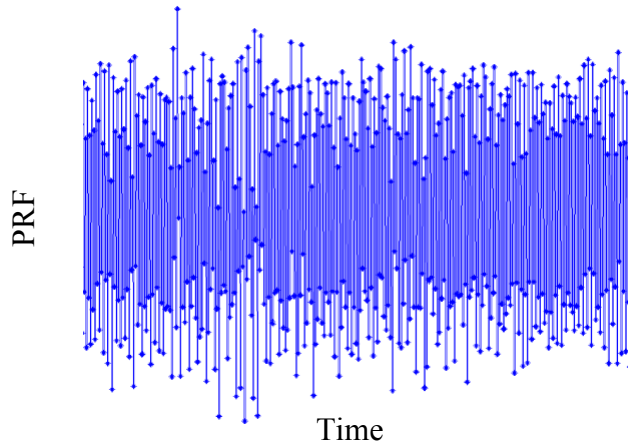

Figure 24: This plot shows an example of the variation in PRF as a function of time.

A first estimate of the angle φ_0 could be found from

$$\varphi_0 = \max(E(P_j)), \tag{13}$$

where

$$E(P_j) = \sum_{i=0}^{n} \left| S(t_{p,j} + i) \right|, \tag{14}$$

n could be related to the pulse width and j spans the number of pulses in a scan. This assumes maximum signal strength for pulse P_j given $\varphi = \varphi_0$.

A second level of fine-tuning has been applied in our experimental set-up. From a set of scans a clutter map was generated for a series of pulses close to φ_0. With this clutter map defined as the true direct direction, correlation is done between this map and the clutter returns from succeeding pulse sets in close vicinity of the estimated φ_0. In Figure 25, the correlation in range and cross range with a clutter map is summed in cross range and plotted as a function of range and shift in time for the pulses. A well-defined correlation top is observed for one time instant, that is when the sum in range is maximum. This is used as the new fine-tuned φ_0 for this scan. An error in the initial definition of the direction of the clutter map, results in a constant bias in direction. Knowledge of strong clutter returns that could be mapped to structures in a real map could help in avoiding biases.
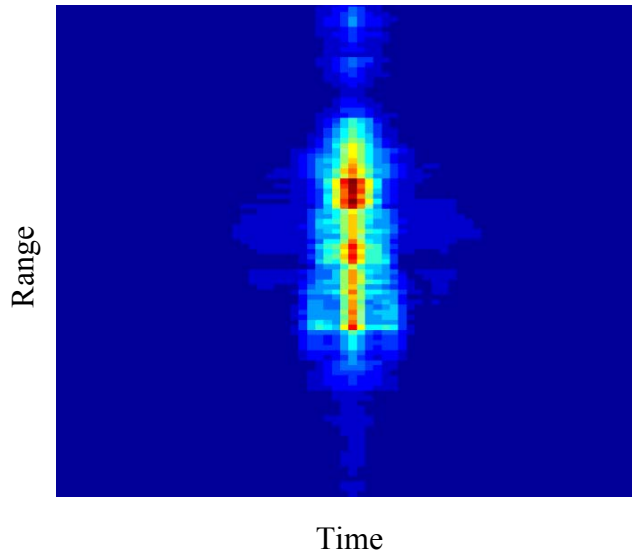
**Figure 25: Fine tuning of direct pulse angle estimation by use of correlation
of clutter map with samples from pulses around φ_0 at each scan.**

For a series of scans, the filtered signal representing clutter and targets are displayed in Figure 26 centred on the direct pointing pulse P_0. Non-coherent integration of a number of N pulses was used in the processing. Target tracks can be seen as curved lines in the lower centre part of the plot.
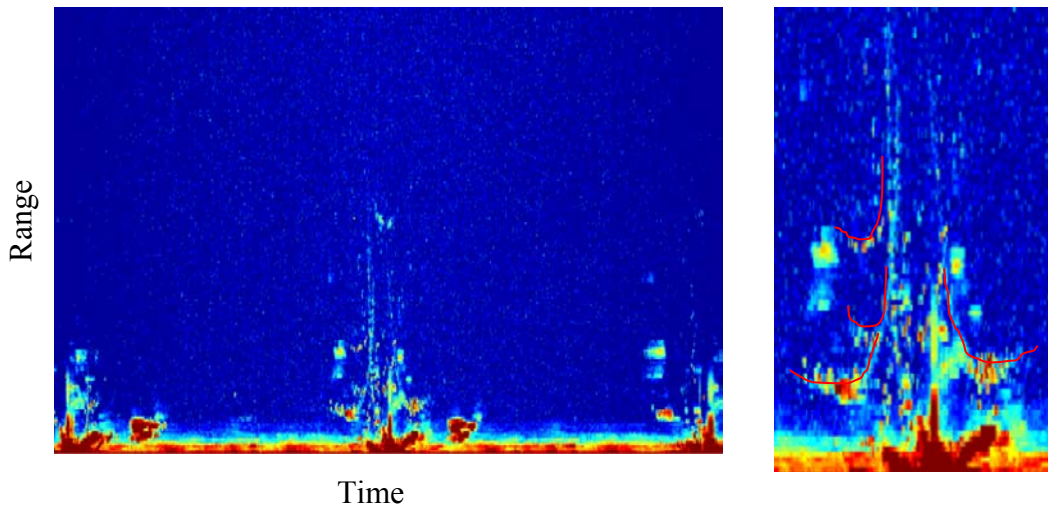

**Figure 26: Cumulative plot of processed signals centred around P_0 and plotted
in range as a function of processed sample index after $t_{p,j}$. In the magnified
view to the right traces of passing planes are indicated by red lines.**

The scan period, pulses per period and P_0 are found from analysis of sampled data corresponding to a whole scan of the Tx antenna. Since we don't have elevation information, we assume all targets are in the same bistatic plane. The plotting of the filtered signal onto a north-east map is possible from knowledge of $\varphi(t)$, $t_{p,j}$ and radar positions. An example of such a plot is shown in Figure 27. To the left, the processed signal is plotted in a cumulative plot with a decay factor implemented to allow for old tracks to fade away. The blue interior ellipse bounded area come about from the radar being blind for a given excess time after the arrival of the direct pulse-front. The size of the area is related to the pulse width and filtering applied in

the processing. This blind zone is drawn in the bistatic plane, here the horizontal plane, while objects at higher altitudes might be detected but not correctly positioned as indicated in Figure 21. To the right in Figure 27 a clutter map has been generated from a series of scans and subtracted from the processed data prior to plotting. This cumulative plot shows several tracks within the processed data window inside the circle. Further processing could be applied to generate tracks in 2D space with estimates of track state vectors.
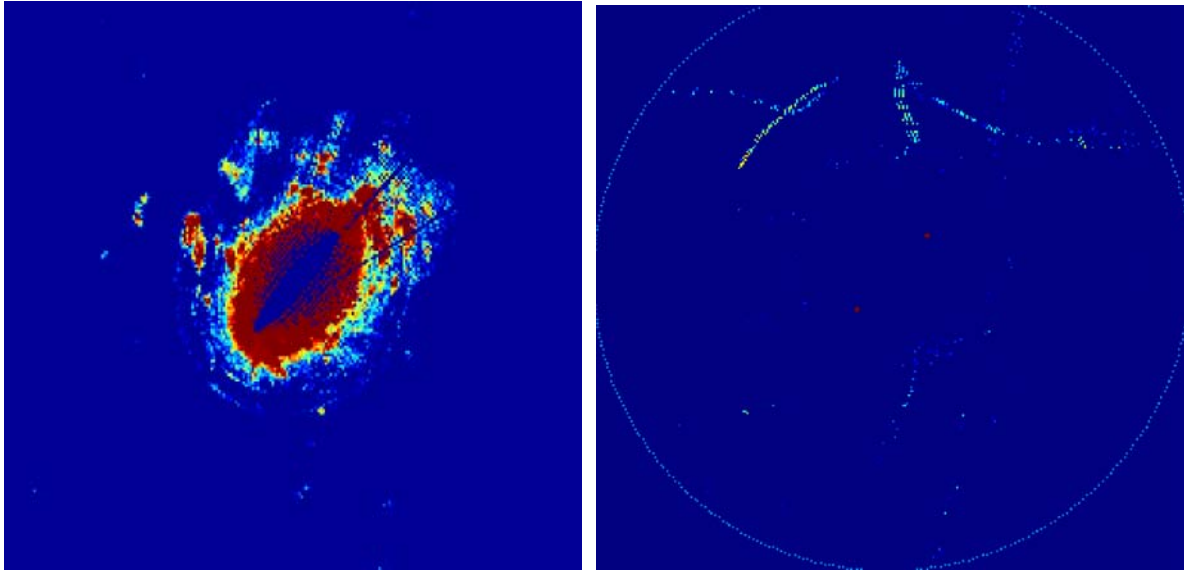

Figure 27: Left: Plot of processed bistatic data in 2D corrected for angle of transmission.
Right: A clutter map has been generated and subtracted from the processed bistatic data.

4.2 Bi- and Multistatic Radar with Controlled Tx

An experimental multistatic radar has been developed at FFI in recent years [6][7] that apply range-gated Continuous Wave (CW) Doppler processing. The CW radar has low output power, and is believed to have Low Probability of Intercept (LPI) properties. It uses an operator selectable binary pseudo random noise code of length *M,* which is modulated onto the carrier by use of binary phase shift. The processing of the sampled radar data into range-Doppler space use similar processing as traditional monostatic radar. It is in the interpretation of these processed results into quantities such as location, velocity and heading that it differs.

The experimental system consists of two transmitters and one receiver unit that are all synchronized in frequency and time by use of local reference oscillators disciplined to GPS. That is, the receiver knows the time of code/pulse transmission with uncertainty given by the GPS receivers 1 Pulse Per Second (1PPS) uncertainty. The carrier frequency is $f_{Tx} = 5.9 GHz$ and the code bit frequency used is $f_{bit} = 5 MHz$. In the processing set-up, the number of code sequences *A* to process in each block is specified. With a code length of *M*=936 bits and processing block of *A*=128 codes the PRF, maximum unambiguously velocity and velocity resolution are

$$PRF = \frac{f_{bit}}{M} = 5.3 kHz \tag{15}$$

$$v_{max} = \frac{cf_{bit}}{2f_{Tx}M} \approx 136 m/s \tag{16}$$

and

$$\Delta v = \frac{v_{max}}{A} \approx 1.1 m/s \tag{17}$$

This selection of A and M corresponds to coherently processing a time interval of $T \approx 25ms$. The unambiguous bistatic range could not be uniquely defined, but depends on the geometry and lobe patterns [1].

In the experimental version, horn antennas with beam widths of approximately 20x20 degrees are used as shown in Figure 28. The video camera on the top is used for tracking a target in a remote located control room.
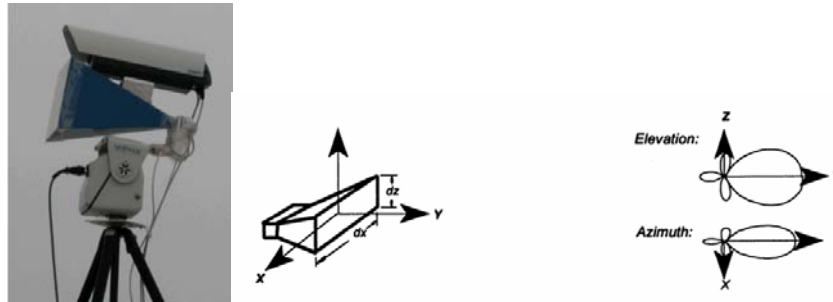

Figure 28: Antenna and co-located video camera used in Tx and Rx mounted on a tripod with tilt and pan. To the right is shown a sketch of antenna lobe pattern for a horn antenna.

A possible use of such a radar system could be as gap filler covering e.g. a valley or fjord with a narrower beam width on the receiver as sketched to the left in Figure 29. If both Tx and Rx uses high gain antennas, it results in geometry dependent common main lobe volumes with a bistatic range spanning an interval $[R_{min}, R_{max}]$ as illustrated to the right in Figure 29. Assuming no echo returns are received in the side-lobes, the unambiguous bistatic range is given by the interval and the bistatic PRF could be increased to

$$PRF_b = \frac{c}{R_{max} - R_{min}} \tag{18}$$

and consequently, in our case of CW, a shorter code length must be used. With a number of directions to scan, a geometry adjusted PRF would reduce the revisit time. According to (16) and (17) this leads to a reduced velocity resolution which could be unacceptable. The use of CW reduces the energy of the signal processed coherently unless A is increased.
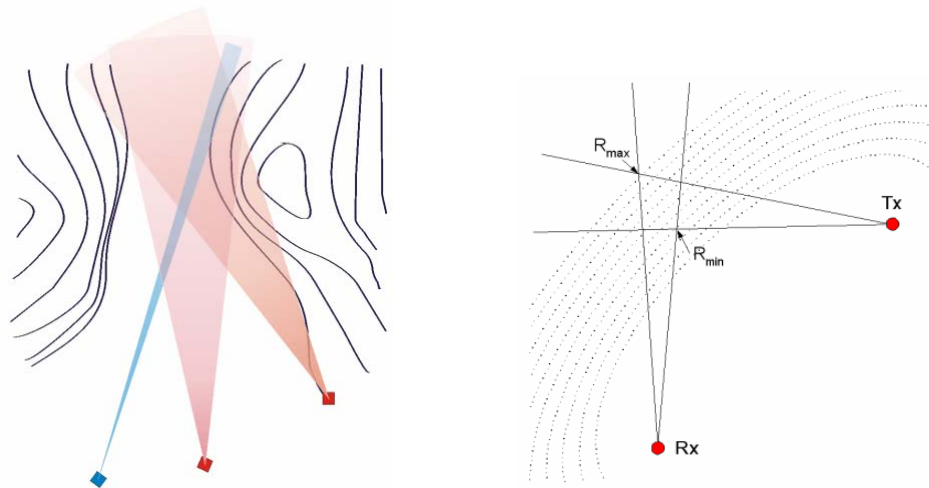
**Figure 29: Left: Example of a multistatic gap filler with a reduced Rx antenna lobe
width to get more accurate angle measurements. Right: Common cross
section area of Tx and Rx antenna lobes with a bistatic range interval.**

With more than one transmitter in multistatic radar, the transmitters must be distinguished either in choice of code or separated in frequency [8]. The cross-section for two bistatic radar pairs as shown to the left in Figure 30 are not equal, unless co-located. The processing could result in ambiguities with respect to bistatic range and velocity if both Tx transmits similar code at the same frequency. Similar codes could be allowed if the lobe directing algorithms ensure separated bistatic range intervals as exemplified in the plot to the right in Figure 30.
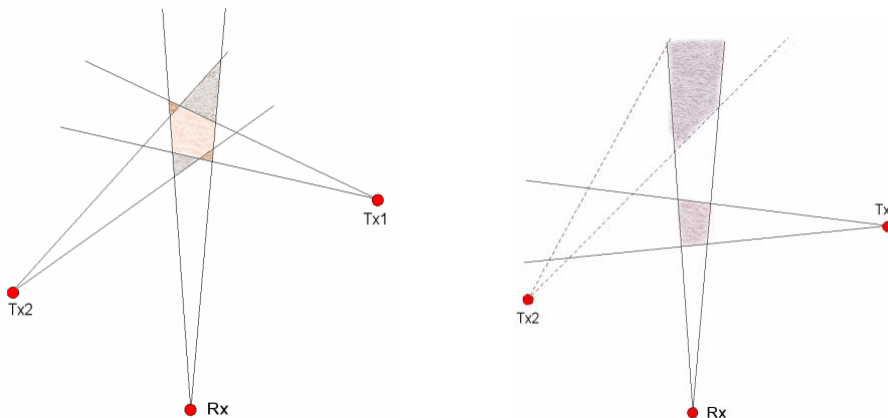

**Figure 30: Left: Cross-section of two Tx-Rx pairs in a multistatic radar pointing to the
same position typically don't coincide. Right: Organisation of detection volumes
of two bistatic radar pairs such as to have separated bistatic range intervals.**

The experimental multistatic receiver has been designed with two separate receiver chains as shown in Figure 32 for each of the two transmitters operating at well-separated frequencies. A simulation study [8] has shown that a separation of approximately 1.5 the signal bandwidth would allow using the same code sequence as seen in Figure 31. The interference of the other Tx on processing signal returns from the first Tx is found to be small. There is no coherent processing of signals resulting from the two receiver chains.
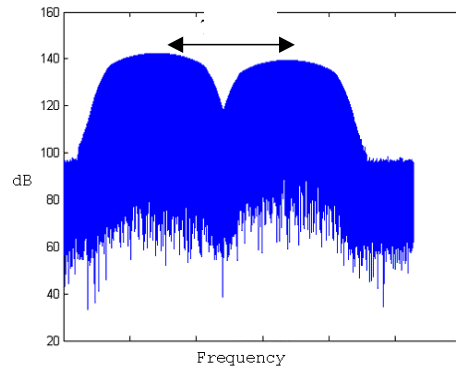
Figure 31: Plot of received signal with two transmitters used with a separation of approximately 1.5 times the signal bandwidths.
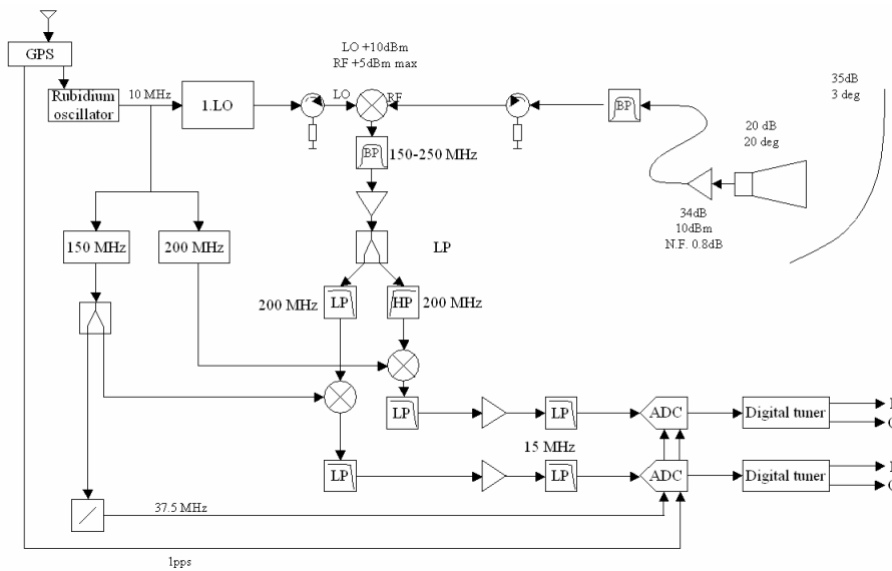

Figure 32: Detailed description of multistatic receiver with two receiver chains.

4.2.1   Experimental Results

A series of trials have been executed with targets ranging from reference plates and cars to helicopters and planes of various types, either targets of opportunity or dedicated objects. An example Range-Doppler plot of a passing airplane is shown in Figure 33. The geometry of Tx and Rx is shown to the left. For these measurements we have the same situation as analysed for the track profile P1. With $R>L$ we see the similarity in range-Doppler profile with the track with largest separation to baseline in Figure 14.
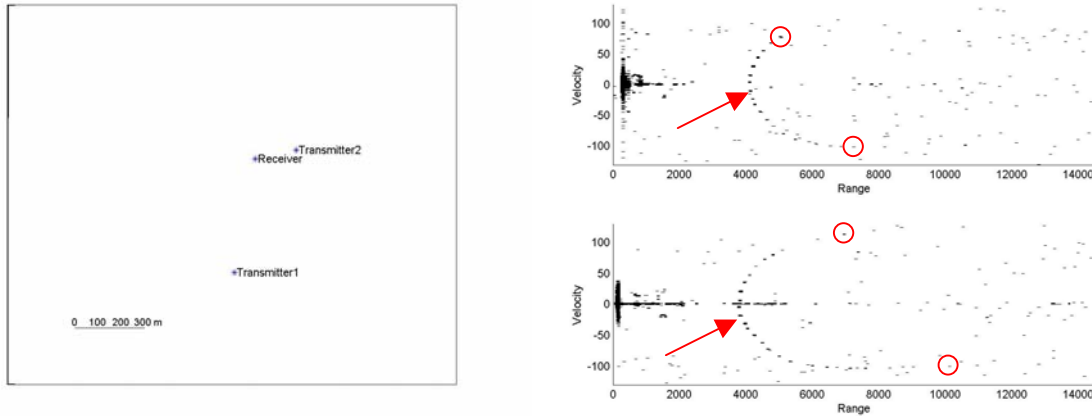
**Figure 33: Left: Geometry of Tx and Rx. Right: Accumulated
track plotted in Range-Doppler for the two bistatic pairs.**

Helicopters and propeller aircrafts result in a Doppler response that spreads out in both velocity directions relative to the body velocity due to the rotating blades. Mono-statically so-called flashes in the backscattered energy occur typically when the blades are oriented perpendicular to the direction of the antenna beam. For these directions the scattering are specular. The tip of a rotor typically has a velocity around 225 m/s. A maximum Doppler shift relative to the Doppler shift of the body is found when the radar beam is in the rotation plane of the rotor. Generally in bistatic radar, the rotor rarely rotates in the bistatic plane, but has an angle between the rotation plane and the bistatic plane. In Figure 34 measurements of a hovering helicopter are shown for $\beta \approx 0$ (left) and $\beta = 33$ (right). For $\beta = 0$, the monostatic case, the large common footprint area of the two beams cause clutter returns from all ranges to bury the scattered signal from the helicopter body. In the bistatic measurement, the common footprint area is reduced and the helicopter body is uncovered in the processing. Theoretical bistatic tip velocities of the two geometries have been calculated to 217 and 207 m/s, respectively. This is close to the values found. The detection of a wide spread Doppler signal can be used as a propeller or helicopter detector.
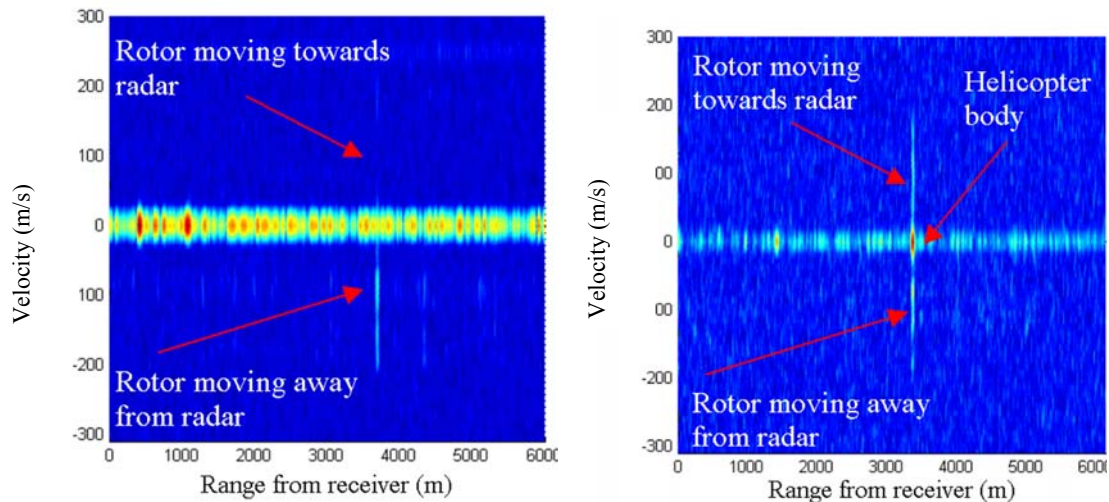

**Figure 34: Accumulated bistatic measurements of hovering helicopter
with rotor blade flashes recorded with $\beta \approx 0$ (left) and $\beta = 33$ (right).**

By processing a number of code blocks *A(t)* as a function of time and extracting the velocity spectrum at bistatic range *R* of the flash, additional quantities can be estimated as shown in Figure 35. The number of rotor blades in the main rotor is an odd number since flashes occur with alternating velocity directions (left plot). For a high bistatic angle measurement of β=127 shown to the right, reminder of the main rotor flashes appear in positive direction together with synchronously Doppler shift lines in both directions originating from tail rotor flashes at a higher rate. Period of rotation and flash durations could be estimated for both rotors. With multistatic radar, the combination of results could in addition identify the direction of rotation from analysis of flash times. In a classification process, input of estimated tip velocities, number of rotor blades, flash duration, rotation period and direction from a set of bistatic entities could be used in multistatic radar.
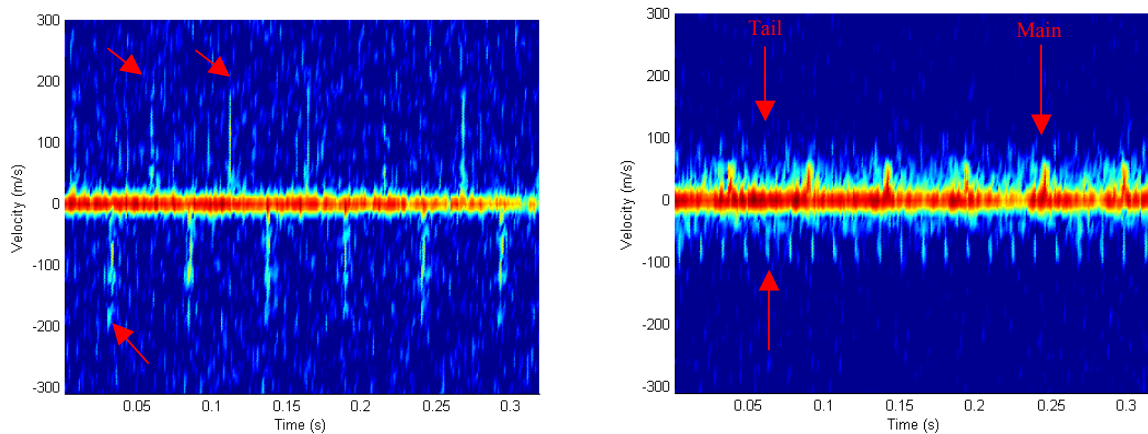

Figure 35: Accumulated bistatic measurements of hovering helicopter with rotor blade flashes recorded with β=33 (left) and β=127 (right) plotted as a function of time.

In a simple RCS simulation using Physical Optics principles (PO), the static spatial RCS distribution of a simulated rotor blade has been calculated for a given geometry as shown in Figure 36 [9][10]. The profile of a blade shown in (a) indicates with colours for different model sections that different orientation reflects energy in different directions (b). The CAD model of the blade (c) is located in the origin with the horizontal blade axis along the y-axis. The spatial RCS distribution in (d) is calculated for a static Tx position (ϕ = 30, θ = 0). The fine pattern seen in (d) is a result of the CAD models finite resolution. As the Rx is located in various (ϕ,θ) positions, we observe the values corresponding to a flash in yellow. As we move Rx in elevation, the position of maximum reflected energy moves towards an increasingly negative azimuth angle. For Rx positions in the xy-plane, the flash is found when the main axis of the rotor blade is perpendicular to a line along the bistatic bisector, that is δ=0. For $|\theta|$ >0 the bistatic angle increases and the bistatic tip velocity is reduced. This corresponds to what was observed for the experiments.
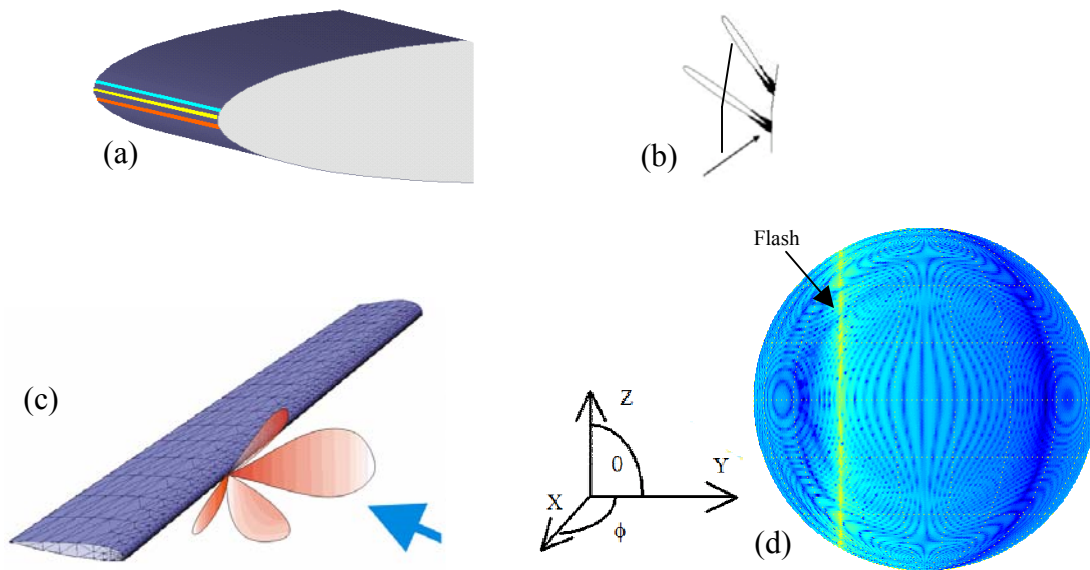
Figure 36: (a) Profile with coloured strips indicating that the reflected flash in given directions result mainly from one section of the rotor blade. (b) Flash direction depends on incoming wave direction. (c) Illustration of MathCAD wing profile used in simulation of RCS. (d) Spherical RCS distribution for wing profile positioned along y-axis and Tx at an azimuth angle of ϕ=30 degrees.

4.3   Bistatic Synthetic Aperture Radar (SAR)

In the previous two systems, ground based Tx and Rx was assumed. Clutter is then received with zero Doppler, which enables simple filtering in the Doppler range. When Tx and/or Rx are located on a moving platform clutter will spread out in Doppler. The Doppler spread in the bistatic range cell is range dependent as well as geometry dependent, which is not the case in monostatic radar. The details of how these iso-Doppler contours depend on platform velocity vector and bistatic geometry can be found in Willis [1]. Methods based on Space Time Adaptive Processing (STAP) have been developed to address the problem of range dependency of the clutter Doppler spectrum in bistatic radar [11].

In addition to conventional broadside and squint mode SAR, forward-looking SAR is possible in bistatic geometries. This enables the receiver to process the signals to produce a SAR image in forward flight direction. Studies have been performed of methods to improve the resolution in this mode [12]. Due to β>0, bistatic radars are less affected by strong returns from corner reflectors often found in man-made constructions. This could be favourable for the dynamics in the processed data e.g. in a bistatic SAR image.

To focus the image, phase distortion must be compensated and recording and communication of motion compensation must be established between platforms for on mission processing of SAR images. Figure 37 shows an example of an optical image and a bistatic SAR image taken of the same area.
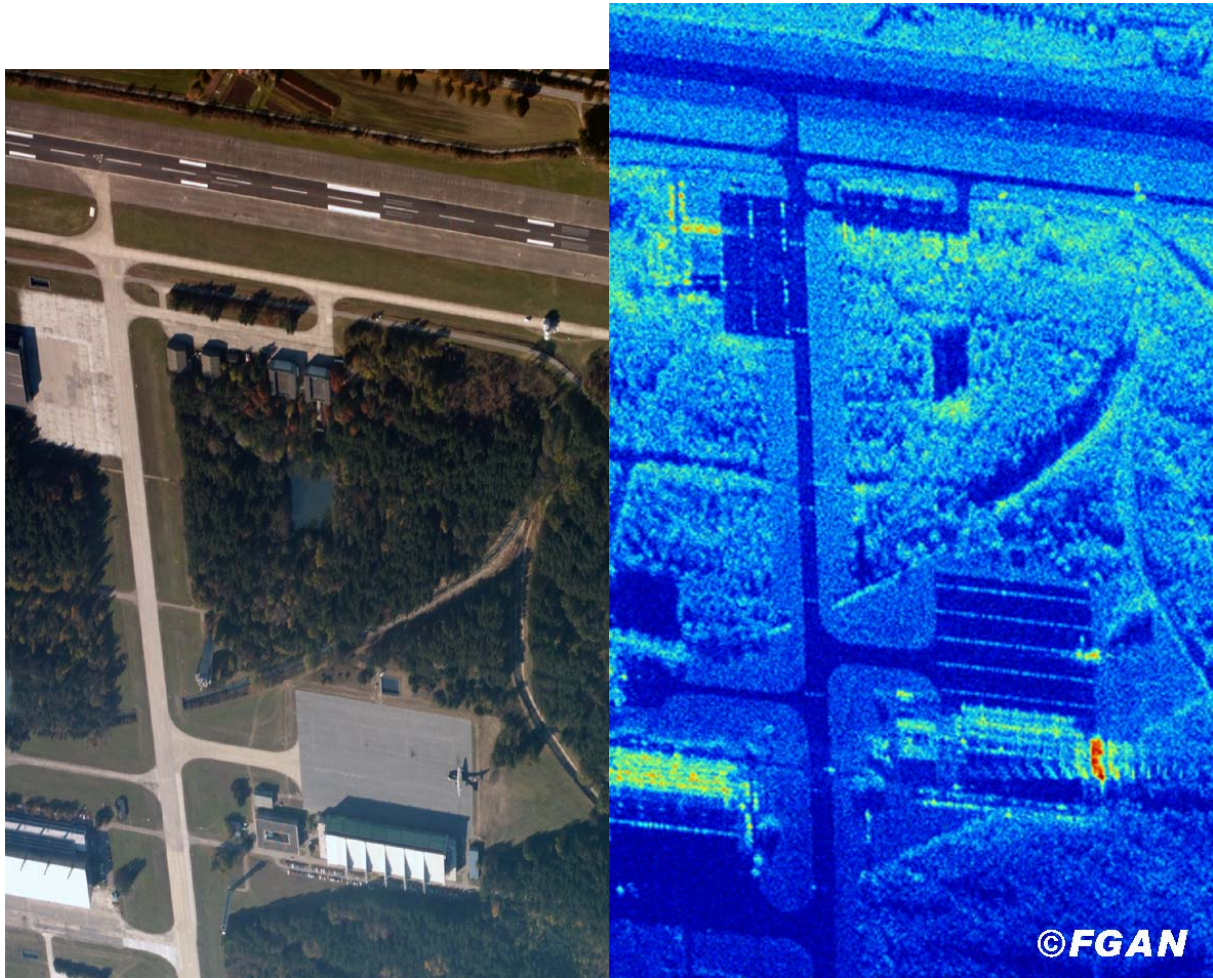
**Figure 37: Example of optical image and processed bistatic
SAR image of the same area. (© FGAN, Wachtberg)**

The bistatic SAR image was recorded with β=29°. The resulting bistatic SAR image shows a part of an airfield with a runway at the top, some taxiways, bushes and two hangars. The optical image is useful for comparisons. For example, remarkable is the different paving of the runway, which is observable by the different brightness. Further the strong reflections in front of the right hangar are not visible in the optical image. The grids for run-off rainwater are the cause of these strong reflections.

5.0   BI- AND MULTISTATIC RADAR DATA AND TRACKING

If no information of angle is measured, the target position is located on an isorange ellipsoid interval defined by the isorange uncertainty and the measured range sum R. If several bistatic radar pairs detect one target, a better position estimate can be found from the intersection of the ellipsoids as indicated in Figure 38. Depending on the location of systems and target position the ellipsoids will result in a more or less well defined intersection volume/area. When there are several targets, the correct association of measurements from all radar pairs and discarding the ghost targets of wrong combinations is not trivial [13]. For a bistatic radar based on television broadcast signals, tracking from bearing and Doppler measurements has been shown by Howland [14]. In the rest of this section we will restrict the discussion to systems where measurement angle information is available, as is the case for the two ground-based experimental systems discussed previously. An example is presented that uses state-of-the-art IMM

filtering with bi- and multistatic simulated radar input with two different approximation methods of the measurement uncertainty.
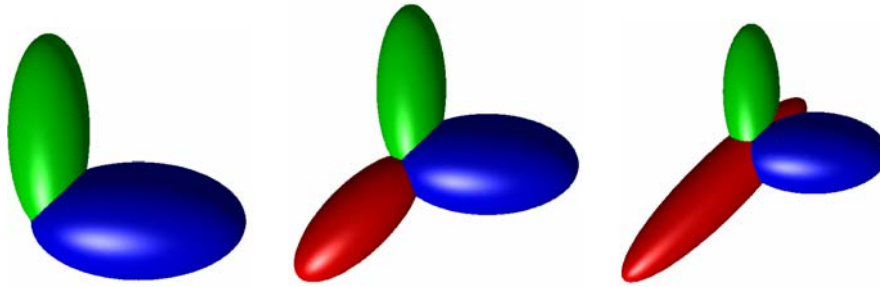

Figure 38: This plot shows an illustration of isorange contour ellipsoids for two and three bistatic radar pairs. Common points of the ellipsoids are candidate positions of a common detected target.

5.1   Measurement Uncertainty Approximation Method-1

The measurement uncertainty region is geometry dependent in bistatic radar. In a Kalman Filter based tracking filter, an expression of this quantity is used. In a North-East-Down (NED) coordinate system with the baseline along the East-axis, R_R could be written as [1]

$$R_R = \frac{(R_T + R_R)^2 - L^2}{2((R_T + R_R) - L\cos(\theta_A)\cos(\theta_E))} \tag{19}$$

where θ_A and θ_E are the azimuth and elevation angle of the receiver bore sight direction of the antenna as defined in Figure 39. Equation (19) is based on [1] (pp. 86) inserted the azimuth and elevation angles of a directive antenna.
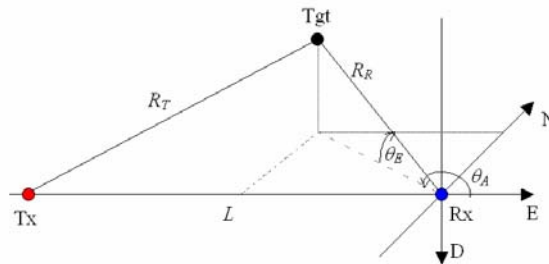

Figure 39: Definition of the θ_A and θ_E angles in a bistatic geometry drawn in a North East Down (NED) coordinate system.

The uncertainties σ_R, σ_A and σ_E in the measured quantities R, θ_A and θ_E are for most bistatic geometries not orthogonal as indicated in Figure 40 (a). Instead, we can use the deduced receiver-target range R_R as a range measure. Measurement uncertainties in these measures are labelled σ_A, σ_E and σ_{RR}. These are orthogonal measures as shown in Figure 40 (b), but σ_{RR} depends on θ_A, θ_E, L and R. Calculating the partial derivatives of R_R
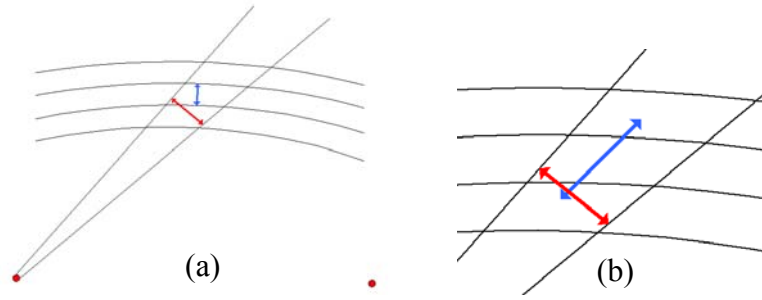
**Figure 40: (a) Illustration of 3σ uncertainties in range sum and
azimuth angle. (b) Orthogonal uncertainties in azimuth and R_R.**

with respect to the dependent variables and summing their contribution using the root-sum-square, an expression for the measurement uncertainty in R_R is found by

$$\sigma_{R_R} = \sqrt{\left(\frac{\partial R_R}{\partial R}\sigma_R\right)^2 + \left(\frac{\partial R_R}{\partial L}\sigma_L\right)^2 + \left(\frac{\partial R_R}{\partial \theta_A}\sigma_{\theta_A}\right)^2 + \left(\frac{\partial R_R}{\partial \theta_E}\sigma_{\theta_E}\right)^2} \tag{20}$$

where σ_L is the uncertainty in L. For a ground based system, this error is usually small and GPS position uncertainties could typically be used. As a first approximation to the measurement uncertainty these quantities were used as method-1. Two examples of measurement uncertainty ellipses for two different geometries are shown in Figure 41. The left plot shows poor correlation, while in the geometry to the right the regions are more compatible.
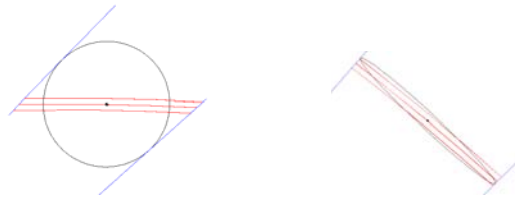

**Figure 41: These figures show part of the range sums R ellipses with uncertainty
in red and corresponding angle uncertainty in blue. The modelled measurement
uncertainty ellipses for two different geometries are shown.**

5.2   Measurement Uncertainty Approximation Method-2

To get a better estimate of the uncertainty region, a second approximation method named method-2 based on Cramer-Rao Lower Bounds (CRLB) methods was used. From the non-linear measurement function, partial derivatives are formed locally at the estimated target position, generating the measurement matrix D. The approximation of the Cartesian measurement covariance matrix W is found by inverting the Fischer information matrix

$$W = \left[D^T P_w^{-1} D\right]^{-1}, \tag{21}$$

where

$$D = \begin{bmatrix} \partial f_A/\partial x & \partial f_A/\partial y & \partial f_A/\partial z \\ \partial f_E/\partial x & \partial f_E/\partial y & \partial f_E/\partial z \\ \partial f_R/\partial x & \partial f_R/\partial y & \partial f_R/\partial z \end{bmatrix}, \quad P_w^{-1} = \begin{bmatrix} 1/\sigma_A^2 & 0 & 0 \\ 0 & 1/\sigma_E^2 & 0 \\ 0 & 0 & 1/\sigma_R^2 \end{bmatrix} \tag{22}$$

f_A, f_E and f_R are the measurement functions in azimuth, elevation and range sum, respectively. P_w represents the radar measurement noise matrix. The measurement errors are assumed to be Gaussian. An example that shows the closer approximation to the uncertainty region in the range-azimuth plane by projection of the 3d error ellipsoid is shown in Figure 42. The ellipse is drawn with 3σ.
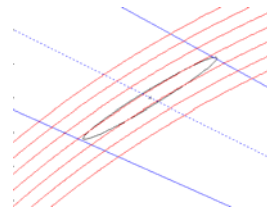

**Figure 42: Example of measurement covariance shown by the ellipse
for approximation by method 2 in the azimuth-range plane.**

5.3   Tracking Simulation

To observe the effect on the tracking of using either method-1 or 2 in computing the measurement covariance matrix, a single track T1 has been generated with a velocity of 300 m/s. T1 has a track path consisting of straight-line segments and curves with a maximum acceleration of 5g in a plane of constant height z=0. Two bistatic radar systems have been located parallel as shown in Figure 43. A tracking filter has been implemented by use of an Interacting Multiple Models (IMM) algorithm, consisting of two simple 2. order Extended Kalman Filter (EKF) models as illustrated in Figure 44. There are one non-manoeuvring and one manoeuvring target model in the IMM filter.
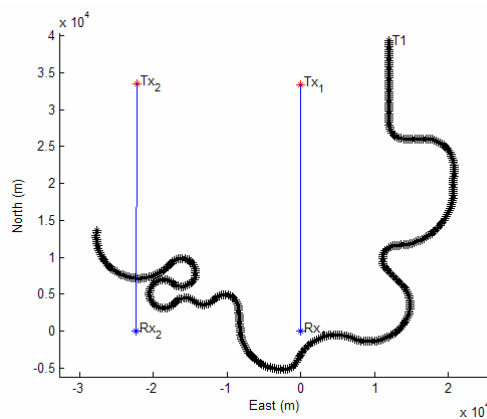

**Figure 43: Simulated track profile and positions of two
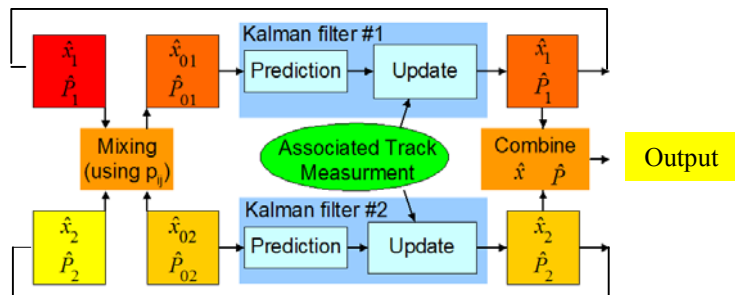bistatic radar systems labelled T_{x1}-R_{x1} and T_{x2}-R_{x2}.**

Figure 44: Illustration of a two-model IMM filter.

The 3σ uncertainties are set to 5 degrees in azimuth and elevation and 32 meter in *R* for the simulation. Measurements are simply generated by use of the true values added noise given by the measurement uncertainties. This optimistic approach assumes that some sort of monopulse or sequential lobbing is used to provide angle information. The initiation or deletion of tracks is not part of the simulation. Perfect tracking capability is assumed. A Monte Carlo run was executed with the use of approximation method-1 and 2 with input of either one or two bistatic radars (multistatic radar). The number of measurements was held constant by using twice the measurement rate when one bistatic radar input was used. In Figure 45 and Figure 46, the average offset from the true target position in distance, velocity and heading are plotted as a function of sim_{index} for all combinations. This index represents an increasing value in the process noise of the manoeuvring model, which can be viewed as a filter tuning exercise [15]. From the results of this single-track simulation, the multistatic radar has the overall best performance for the given measures when used with the measurement covariance approximation method-2.
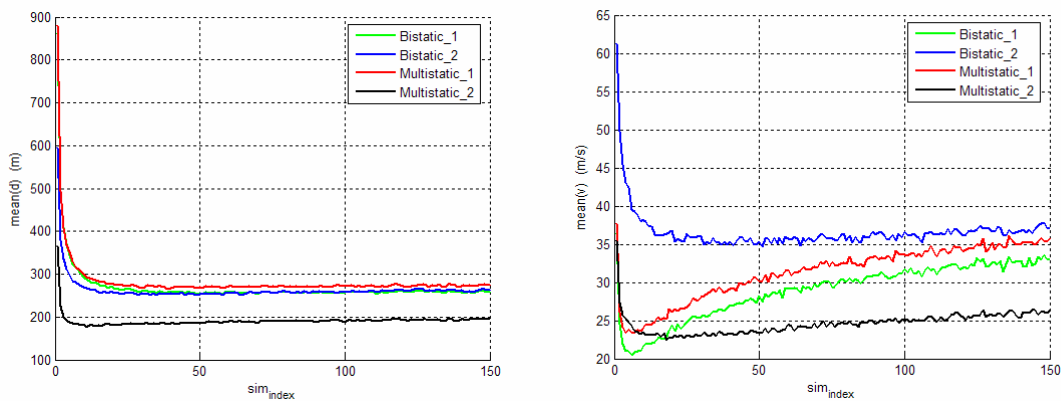

Figure 45: Mean distance offset (left) and mean velocity offset (right) as a function of sim_{index}. The legend subscript _1 and _2 refers to approximation method 1 or 2.
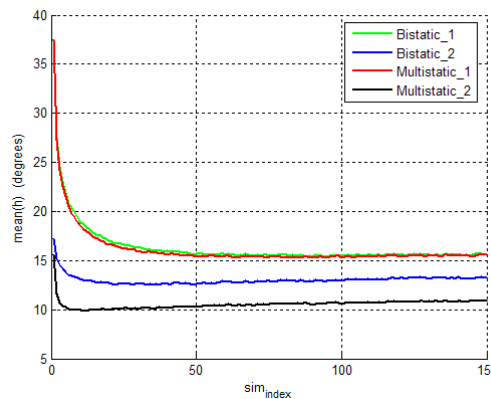

Figure 46: Mean heading offset as a function of sim_{index}. The legend subscript _1 and _2 refers to approximation method 1 or 2.

6.0   SUMMARY

Bi- and multistatic radar are expected to benefit from their separation that denies receiver recognition by ARM, favours covered operation by their silent receivers, has higher detection possibilities of stealthy object and are less vulnerable to jamming. The separation introduces geometry dependencies in range and

velocity components (Doppler) that are important to understand and incorporate in the processing. The constant S/N ratio contours defined by the Cassini ovals define regions of operation that are unique to bistatic radar systems. A set of different track paths relative to the position of a bistatic radar system was studied, and their characteristic appearance when processed by bistatic radar was discussed. The additional requirements of stable references in time and frequency in all units have been discussed. Proper synchronization is essential to give reliable target position and velocity. Processing has been discussed with examples collected from two different types of ground-based bistatic radars. Extraction of various target parameters was shown. The use of moving Tx and/or Rx platforms introduces Doppler spreading and additionally geometry dependent relations. An example of bistatic SAR imaging was presented. Extracting track data that can be viewed in 2D or 3D requires in the case of omnidirectional antennas where no angle information is recorded, the combination of detections from several bistatic systems to identify possible object locations. For antennas with restricted lobe widths, a less uncertain target position is defined. Measurement uncertainties are geometry dependent in bistatic radar. Two different approximation methods were discussed, and results from a simulation was shown that compared tracking capabilities with an IMM filter when one or two bistatic radar inputs were used. Best performance was obtained when two bistatic radar sources were input to the filtering process and the approximation of the measurement covariance matrix was closer to the radars uncertainty volume for all target geometries.

7.0   REFERENCES

[1]   N.J. Willis, Bistatic Radar, British Library, 1995.

[2]   D. Poullin, "On the use of COFDM modulation (DAB, DVB) for passive radar application", RTO SET panel conf. On Passive and LPI Radio Frequency Sensors, Warsaw, 2001.

[3]   K. Kvernsveen, H. Øhra, "Exploitation of Future Broadcast Transmitters for Radar Detection and Tracking", RTO SET panel conf. On Passive and LPI Radio Frequency Sensors, Warsaw, 2001.

[4]   "Super Radar, Done Dirt Cheap", BusinessWeek, October 20, 2003.

[5]   E.W. Weisstein, Cassini Ovals, MathWorld—A Wolfram Web Resource, http://mathworld.wolfram.com/CassiniOvals.html.

[6]   K.E. Olsen, T. Johnsen, S. Johnsrud, R. Gundersen, H. Bjordal, I. Tansem, P. Sørnes, "Results from an experimental Continuous Wave Low Probability of Intercept Bistatic Radar – The first steps toward Multistatic Radar", Proc. IEEE Int. Radar Conf., Adelaide, Australia, 2003.

[7]   K.E. Olsen, S. Johnsrud, T. Johnsen, P. Sørnes, I. Tansem, H. Bjordal, L.W. Westad, "Results from an experimental Continuous Wave Low Probability of Intercept Bistatic Radar – The first experiments", Proc. IEE Int. Radar Conf., Toulouse, France, 2004.

[8]   T. Johnsen, K.E. Olsen, S. Johnsrud, R. Skjerpeng, "Simultaneous use of Multiple Pseudo Random Noise codes in Multistatic CW Radar", Proc. IEEE Radar Conf., Philadelphia, USA, 2004.

[9]   T. Johnsen, K.E. Olsen, R. Gundersen, "Hovering Helicopter measured by Bi-/Multistatic CW Radar", Proc. IEEE Radar Conf., Huntsville, pp. 452-459, USA, 2003.

[10] R. Gundersen, R. Norland, "Spatial predictions of the probability of detection of low signature targets using bistatic and multistatic radar systems versus monostatic radar", Proc. NATO-RTO Symposium on Passivs and LPI Radio Frequency Sensors, Warsaw, Poland, 2001.

[11] F.D. Lapierre, J.G. Verly, M. van Droogenbroeck, "New Solutions to the Problem of Range Dependence in Bistatic STAP Radars", Proc.IEEE 2003, Huntsville.

[12] A.K. Löhner, "Improved azimuthal resolution of forward looking SAR by sophisticated antenna illumination function design", IEE Proc.-Radar, Sonar Navig., Vol. 145, No. 2, April 1998.

[13] M. Herberthson, "On determining multiple positions and velocities from bistatic measurements – fast bistatic association in AASR", FOI Report, FOI-R-0815 – SE, Sweden.

[14] P.E. Howard, "Target tracking using television-based bistatic radar", IEE Proc. – Radar, Sonmar Navig, Vol. 146, No. 3, June 1999.

[15] T. Johnsen, B. Hafskjold, K.E. Olsen, "Tracking and Data Fusion in Bi- and Multistatic Radar", Proc. IEEE Radar Conf., Arlington, USA, 2005.